University of Nevada, Reno

Characterization of short-pulse laser-produced fast electrons by 3D hybrid particle-in-cell modeling of angularly resolved bremsstrahlung

A dissertation submitted in partial fulfillment
of the requirements for the degree of Doctor of Philosophy in Physics

by

Lei Chen

Dr. Hiroshi Sawada/Dissertation Advisor

August, 2023

THE GRADUATE SCHOOL

We recommend that the dissertation
prepared under our supervision by

Lei Chen

entitled

Characterization of short-pulse laser-produced fast electrons by 3D hybrid particle-in-cell modeling of angularly resolved bremsstrahlung

be accepted in partial fulfillment of the
requirements for the degree of

Doctor of Philosophy

Dr. Hiroshi Sawada
Advisor

Dr. Roberto C. Mancini
Committee Member

Dr. Jonathan D. Weinstein
Committee Member

Dr. Thomas G. White
Committee Member

Dr. Christopher J. Barile
Graduate School Representative

Markus Kemmelmeier, Ph.D., Dean
Graduate School

August, 2023

ABSTRACT

The interaction of an intense short-pulse laser with a solid target efficiently generates energetic (fast) electrons above the energy of 1 Mega-electronvolt (MeV). Characterization of such high-energy electrons is critical for numerous applications, such as the generation of secondary particle sources, the creation of warm dense matter (WDM), advanced fusion concepts, and intense x-ray radiation for probing complex high areal density objects and inertial confinement fusion (ICF) fusion cores. However, determining laser-driven fast electron characteristics, specifically, electron energy distribution, divergence angle, and laser-to-electron conversion efficiency, has been challenging partly due to complex electron trajectories caused by electric sheath potential, known as electron recirculation. This thesis reports on developing a novel fast electron characterization technique by modeling angularly resolved bremsstrahlung radiations with a three-dimensional (3D) hybrid Particle-in-cell (PIC) code. An experiment using a 50-TW Leopard laser (15 J, 0.35 ps, 2×10^{19} W/cm^2) was carried out to measure bremsstrahlung radiations at two angular positions and escaped fast electrons along the laser axis for two types of targets: a 100-μm-thick Cu foil and a same Cu target with a CH backing (Cu-CH target). A 3D hybrid-PIC code, Large Scale Plasma (LSP), is extensively used in this work to simulate the electron transport within the solid target, including electron recirculation around the target, and the x-ray generation of absolute photon yields. The measurements were fitted with a series of simulations by varying all three electron parameters. Fitting results based on chi-squared analyses show good agreements for both target types when the electron slope temperature of 0.8 MeV, the divergence angle of 70°, and the electron beam energy of 1.3 J are used.

Furthermore, the effects of electron recirculation on bremsstrahlung generation and the enhancement of a short-pulse laser-produced x-ray intensity in various foil thicknesses are numerically studied. These results provide insight into designing and optimizing an x-ray source target for broadband x-ray radiography of a magnetically compressed aluminum rod at the Zebra pulsed power laboratory.

ACKOWLEDGEMENT

First of all, I am deeply grateful to my advisor, Dr. Hiroshi Sawada, for giving me the precious opportunity to study laser-plasma physics with him and providing numerous resources over the past five years. His continuous advice guided me toward the research goal; his rigorous attitude to work and critical thinking on physics problems have been immensely helpful in my study.

I would like to thank my Ph.D. committee members: Drs. Roberto C. Mancini, Jonathan D. Weinstein, Thomas G. White, Christopher J. Barile, and the previous member Dr.Yiliang Liao for their time and service on the committee. Their thoughtful comments helped to improve this thesis work.

I would like to acknowledge Drs. Vladimir V. Ivanov, Farhat N. Beg, Hui Chen, Anthony J. Link, Gerald J. Williams, Yuan Ping, Harry S. McLean, and ZPPL staff for their support in obtaining the Leopard and Zebra experimental data.

I would like to thank Dr. Tyler. S. Daykin for his help at the beginning of my research.

I thank the former graduate students in Leifson 217, including Jeffrey Rowland, Cameron Allen, Demitri Call, Brandon Griffin, and Alexandar Rollings, for the nice office environment and valuable discussions.

Last but not least, I would like to thank my wife, Xian Zhao, and my daughter Shirley Chen. I love you, and thank you for the priceless and endless joy and love!

This work was supported by the National Science Foundation under Grant No. 1707357 through the NSF/ DOE Partnership in Basic Plasma Science and Engineering. This material is based upon the work supported by the U.S. Department of Energy, Office of Science, Office of Fusion Energy Sciences, High Energy Density Laboratory Plasmas program under Award No. DE- SC0022236.

PUBLICATIONS

1.) **L. Chen** *and* H. Sawada, "*Characterization of sub-picosecond laser-produced fast electrons by modeling angularly resolved bremsstrahlung measurements with 3D hybrid particle-in-cell code*", Physics of Plasmas 29, 093104 (2022)

2.) H. Sawada, J. Trzaska, C. B. Curry, M. Gauthier, L. B. Fletcher, S. Jiang, H. J. Lee, E. C. Galtier, E. Cunningham, G. Dyer, T. S. Daykin, **L. Chen**, C. Salinas, G. D. Glenn, M. Frost, S. H. Glenzer, Y. Ping, A. J. Kemp, *and* Y. Sentoku, "*2D monochromatic x-ray imaging for beam monitoring of an x-ray free electron laser and a high-power femtosecond laser*", Review of Scientific Instruments 92, 013510(2021)

TABLE OF CONTENTS

Page

LIST OF TABLES

Page

LIST OF FIGURES

Page

1. Introduction

1.1 Progress of High-intensity Short-pulse Lasers

Laser, an acronym for light amplification by stimulated emission of radiation, has been widely used in scientific, military, medical, and industrial fields since it was invented in 1960[1]. Nowadays, advanced high-intensity short-pulse lasers play an essential role in physics research and multi-disciplinary applications worldwide. Since Maiman demonstrated the first pulsed laser, significant advances in laser peak power came with the invention of *Q*-switching[2] and then mode-locking[3]. In the late 1980s, the experimental implementation of the Chirped Pulse Amplification (CPA)[4] technique (Nobel Prize in Physics, 2018) offered a revolutionary approach for lasers to reach the intensity threshold of 10^{14}-10^{15} W/cm^2, which corresponds to electric field amplitudes of the same order as the Coulomb field in atoms.

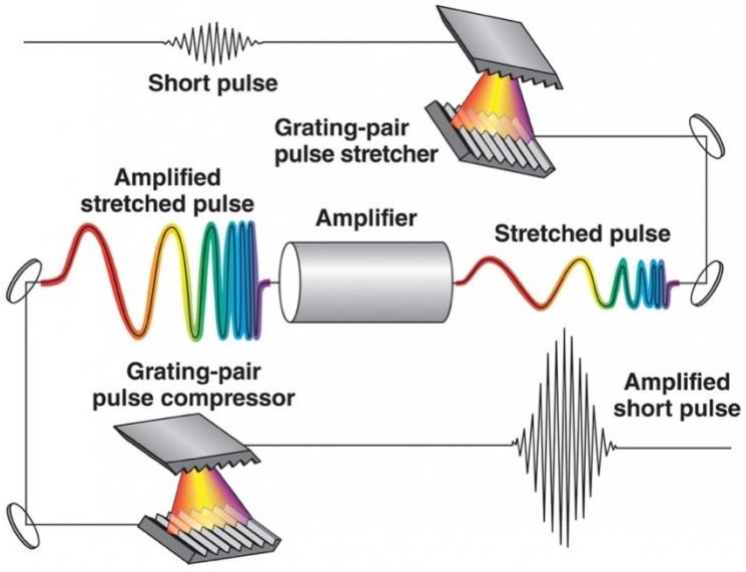

Figure 1.1 Schematic for Chirped Pulse Amplification of a short-pulse laser[5].

The CPA technique, as shown in Figure 1.1, stretches out the initial pulse by a grating-pair pulse stretcher to a long and low-power pulse, which can be safely amplified to a high-power pulse, and then recompress the pulse by a grating-pair pulse compressor to a short length with extremely high intensity. Figure 1.2 shows the historical journey to multi-petawatt ultra-short-pulse laser facilities with significant inventions in laser technique and names of laser facilities. With the CPA technique, short-pulse laser systems can produce laser pulses with a peak intensity above the relativistic intensity of ~10^{18} W/cm^2, while a new important regime in laser-matter interaction is entered: the relativistic regime. Electrons oscillated by such intense electromagnetic fields can reach relativistic velocities within one laser period and experience nonlinear motion under the influence of the Lorentz force. Shortly after the invention of CPA, a hybrid CPA architecture, optical parametric CPA (OPCPA), was first demonstrated by Dubietis et al. in 1992, then practically designed by Ross et al.[6] for large-aperture systems to generate powers in excess of 10 petawatts (PW, 10^{15} W) and focused intensities $> 10^{23}$ W/cm^2. The OPCAP technique is or will be used in constructing several facilities in Europe, the USA, and China.[7]

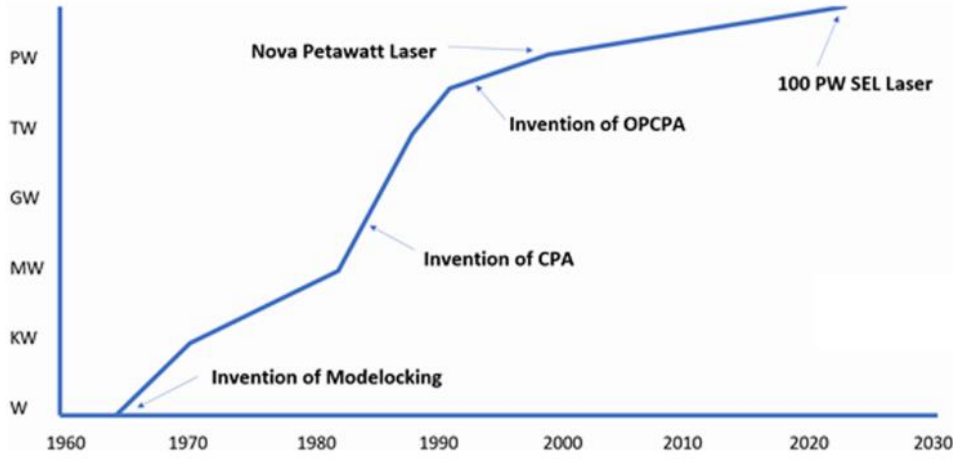

Figure 1.2 The historical journey to multi-petawatt ultra-short-pulse laser facilities[7].

Nowadays, state-of-the-art lasers worldwide routinely deliver unprecedented ultra-high-intensity and high-power laser pulses. For the laser pulse duration, a pulse shorter than 20 fs was first achieved in 2017 at the China Academy of Engineering Physics (CAEP) at a multiple-petawatt laser facility named CAEP-PW[8]. A record peak intensity of $(1.1 \pm 0.2) \times 10^{23}$ W/cm^2 was reported with the Centre for Relativistic Laser Science (CoReLS) PW laser in South Korea by focusing the laser spot to 1.1 μm full width at half maximum (FWHM) with an f/1.1 off-axis parabolic mirror, making strong field QED phenomena possibly to be explored by using this ultrahigh intensity laser.[9] In 2022, laser pulses with a record peak power of up to 10.2 PW at a repetition rate of 1 shot per minute are demonstrated at the Extreme Light Infrastructures Nuclear Physics (ELI-NP).[10] In the near future, the commissioning of even more powerful lasers is underway: A 100 PW-level facility Station of Extreme Light (SEL) in Shanghai is under construction, which will

combine four 30 PW pulses to deliver 1.5 kJ in 15 fs to the target.[11] Meanwhile, in the United States, a 3 PW laser facility at the University of Michigan Zettawatt-Equivalent Ultrashort pulse laser System (ZEUS)[12] plans to commission in late 2023. One of the flagship research activities at the ZEUS facility is to study the interaction of a petawatt laser pulse colliding with a GeV energy electron beam generated by one of its two beamlines to provide the equivalent of a zettawatt (10^{21} W) power laser interaction in the rest frame of the electron beam. Furthermore, a few ultra-intense lasers up to 200 PW are currently planned globally, so a dramatic development of powerful lasers is worth expecting in the next decade.

The work presented in this thesis is based on a series of experiments performed using a high-power short-pulse laser, Leopard, at the Zebra Pulsed Power Lab (ZPPL) of the University of Nevada, Reno (UNR). The Leopard laser[13] is a 50-TW (10^{12} W) hybrid Ti: Sapphire/Nd: glass laser system using both rod and disk amplifiers together with a femtosecond front-end. The laser can deliver 10-20 J of laser energy with a peak intensity of ~10^{19} W/cm^2, above the relativistic intensity (10^{18} W/cm^2), generating energetic electrons (> MeV) near the critical density region in the laser-target interaction. Figure 1.3 shows an overview of the Leopard laser with two vacuum target chambers. The Leopard laser can be used either in a laser-only vacuum chamber called Phoenix or coupled in a Zebra pulsed power chamber. Further discussion on pulsed power-laser coupled experiments in the Zebra chamber at ZPPL will be presented in Chapter 6.

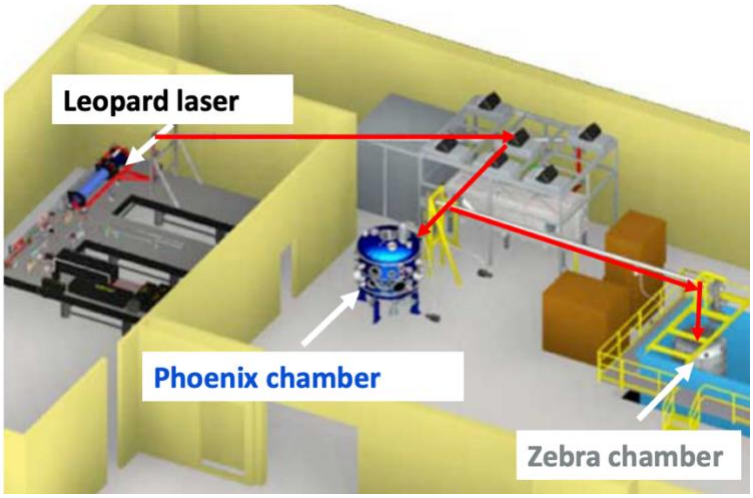

Figure 1.3 Overview of the Leopard laser system and vacuum chambers.

1.2 Applications of High-intensity Short-pulse Lasers

The interaction of an intense short-pulse laser with solid targets generates energetic (fast) electrons and a broadband spectrum of x-ray photons. Laser-produced fast electrons and intense x-rays have been studied for various applications. This subchapter briefly introduces some applications, such as charged particle acceleration, warm dense matter generation by isochoric heating, x-ray and gamma-ray radiation generation, and generation of energetic particles for fast ignition concepts of initial confinement fusion.

1.2.1 Charged Particle Acceleration

The rapid development of intense short-pulse lasers significantly pushes the studies of table-top electron and ion accelerators. For example, the Laser Wakefield Acceleration (LWFA) uses a huge acceleration field created by a high-power laser pulse at a relativistic

intensity propagating in a gaseous medium. This acceleration mechanism can accelerate electrons to multi-GeV with a centimeter-long medium[14]. In contrast, conventional Radio-frequency acceleration technology requires a few hundred meters to generate such a high-energy beam. On the other hand, laser-solid interaction produces a large number of relativistic electrons, which play a crucial role in accelerating protons and ions. Energetic protons and ions can be accelerated by a mechanism called Target Normal Sheath Acceleration (TNSA)[15]. In this case, fast electrons traverse through the solid target and escape to the vacuum while creating a strong static electric field on the back of the target. The strength of the field is as high as TV/m so that protons in a contaminant layer on the target rear surface are ionized and accelerated. Several other laser-driven ion-acceleration mechanisms are working in various regimes with different target thicknesses and densities, such as Radiation Pressure Acceleration (RPA)[16,17], Break-out afterburner (BOA)[18], and Collisionless Electrostatic Shock Acceleration (CESA)[19]. These accelerated high-energy ions (>tens of MeV) are studied for medical treatment[20], ion fast ignition[21], and the generation of high-energy neutron sources[22]. Figure 1.4 shows RPA and TNSA acceleration mechanisms with a thick (much thicker than the skin layer) target.

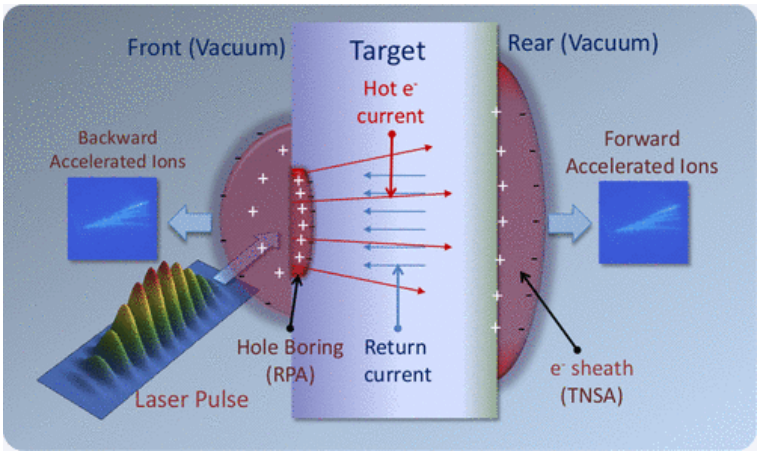

Figure 1.4 A cartoon showing acceleration mechanisms of TNSA and Hole Boring (RPA) in the interaction with a thick solid target.[23]

1.2.2 Generation of the Warm Dense Matter

Warm Dense Matter (WDM) is a state of matter which lies between condensed matter (solids and liquids), gases, and ideal plasma. Matters in this regime have a density from near solid density to 10 times its values and a temperature from a few eV to 100 eV (1 eV = 1.16×10^4 K). WDM is commonly found in astrophysical objects and the core of an inertial confinement fusion implosion[24]. WDM is a rapidly developed field of physics since it is a meeting point of several distinct physical regimes and not a simple extension of well-developed models of adjunct regions in the density-temperature space. The creation and diagnosis of WDM in laboratories are crucial to validate theoretical models for WDM. Figure. 1.5 shows an experimental setup for WDM generation by irradiating a short-pulse laser to a wire target. When irradiating an intense short-pulse laser on planar[25] or wire[26] targets, the high density of the target is maintained during the delivery of energy since the laser pulse duration is much shorter than the time scale of hydrodynamic expansion. Laser-produced fast electrons can effectively deposit their energy to the material by isochoric heating as they propagate into the target. The isochoric heating may increase the temperature of material up to 100-1000 eV, which is in the WDM or hot dense matter.

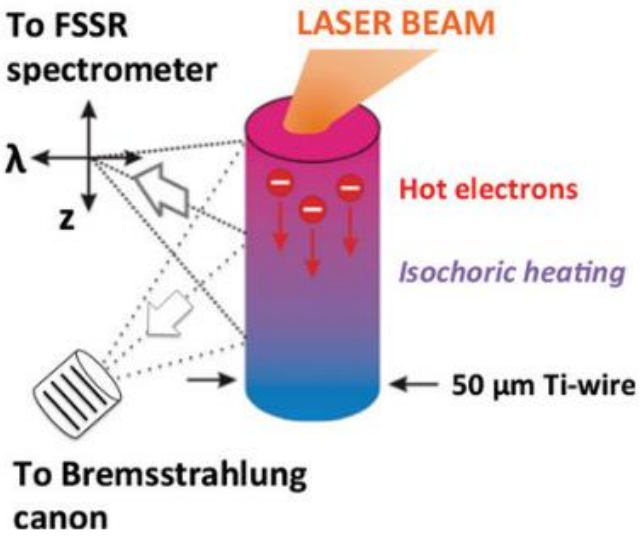

Figure 1.5 An experimental setup for Ti-wire target generated WDM.[26]

1.2.3 Inertial Confinement Fusion

Inertial Confinement Fusion (ICF) is one of the two main branches of controlled thermonuclear fusion research, and the other is Magnetic Confinement Fusion (MCF). Direct-drive and indirect-drive ICF uses high-power laser beams to compress a spherical pellet filled with fusion fuels to ignition conditions. The compressed target forms a hot spot surrounded by a cold high-density fuel at the stagnation, initiating thermonuclear reactions and the propagation of thermonuclear burn waves to continue burning the dense fuel[24]. The most favored (largest cross-section) fusion reaction is the deuterium(D)-tritium (T) fusion [D + T → *n* (14.1 MeV) + ^{4}He (3.5 MeV)][27]. Figure. 1.6 illustrates typical concepts of ICF: indirect drive, direct drive, and fast ignition (FI). In the direct drive concept, which is also called central hot spot ignition (CHS), symmetrically arranged laser beams irradiate a fuel

capsule. Ablation of the capsule surface drives shockwaves, which compresses the capsule to form a low-density, high-temperature hot spot surrounded by a high-density fuel at the stagnation. Once the hot spot reaches the Lawson criteria (areal density > 0.3 g/cm^2) with an ion temperature of > ~ 5 keV, thermonuclear fusion takes place in the hotspot. Alpha particles produced in the hot spot heat the fuel layer, which triggers a propagation of a thermonuclear burn wave for the self-sustaining fusion reaction. The coupling efficiency is relatively higher than other concepts in the CHS scheme. However, the hot spot formation is challenging because of hydrodynamic instabilities that cause the mixing of the cold fuel layer into the hot spot, cooling the hot spot temperature.

The indirect drive scheme differs from the direct drive scheme by using the laser-produced x-rays in a high-Z hohlraum to drive a fusion fuel target, and it relaxes the requirement of laser beam uniformity and reduces hydrodynamic instability during the compression. As shown in Fig.1.6 (a), a spherical capsule containing DT fuel (DT gas inside a DT ice shell) is placed inside a gold cylindrical hohlraum, and high power lasers are injected in multiple directions and generate x-ray radiation on the interior wall of the hohlraum. The laser-generated x-rays then ablate the capsule's outer surface (a high density carbon ablator layer) and implode the DT fuel via rocket motions. The indirect drive concept is used in the world's largest ICF facility, the National Ignition Facility (NIF) at Lawrence Livermore National Laboratory (LLNL). In August 2022, NIF used 192 laser beams with an energy of 1.92 MJ in an indirect drive implosion to achieve 1.37 MJ fusion energy (Target gain=E_{fusion}/E_{laser}=0.72) in a gold-lined depleted uranium hohlraum.[28] Later, on Dec.5, 2022, an implosion at NIF generated 3.15 megajoules (MJ, 10^6 J) fusion energy

output from a 2.05 MJ laser energy input, reaching the scientific energy breakeven for the first controlled thermonuclear fusion experiment to exceed the gain of unity.[29]

In contrast to the CHS scheme, the FI scheme proposed by Tabak[30] in 1994 uses an additional intense short-pulse laser for achieving ignition. As shown in Fig.1.6 (c), the fuel assembly of the FI scheme is the same as the CHS. However, instead of forming a hot spot, a high-intensity ignition laser is used to ignite the pre-compressed fuel by a beam of energetic charged particles. One of the advantages of FI is that the beam illumination uniformity and compression symmetry requirements are relaxed. In addition, the FI target could produce a high fusion gain (G>100) because the energy of the compression laser can be reduced. It is predicted that fast electrons with energies between 1-3 MeV are desirable for efficient energy deposition to a dense fusion fuel[31].

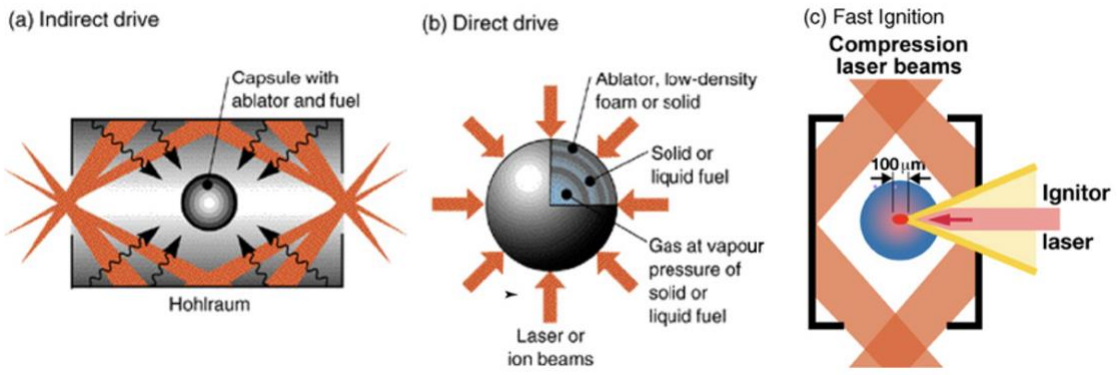

Figure 1.6 Illustration of ICF concepts (a) indirect drive, (b) direct drive, and (c) fast ignition.[32]

However, the FI scheme has its own challenges. One of the critical issues is the generation of preplasma. A low-intensity pedestal before the main ignition laser produces low-density plasma. A long-scale length of the preplasma prevents the laser from propagating close to the core so that a beam of charged particles generated near the critical density is far away from the core, and most diverging fast electrons cannot reach the core. To shorten the standoff distance between the fast electron's generation position and the high-density core, it is proposed to use a laser beam to drill a hole through the coronal plasma around the core region, called the hole boring concept. Another electron FI concept proposed by Kodama et al.[33,34] uses a high Z (usually gold) cone to maintain a plasma-free area for the propagation of an ignition laser (cone-guided FI). Since the ignition laser directly interacts with the cone tip, this scheme could significantly minimize the stand-off distance and enhance the coupling efficiency of the electrons to the core. Another issue of FI is the large divergence angle of the electron beam, which lowers the laser-to-target coupling efficiency. To mitigate diverging electrons, laser-driven magnetic fields of hundreds of Tesla are proposed to guide the relativistic electron beam.[35,36] Other charged particle beams considered for FI include protons and heavy ions. As described in 1.2.1, energetic protons accelerated by mechanisms such as TNSA could deposit their energy into the fusion fuel for ignition.[37]

1.2.4 Short-pulse Laser-based X-ray Radiography

Broadband and characteristic X-ray radiation generated in the interaction of an intense short-pulse laser with a solid target have been used for diagnosing an ICF implosion

core and High Energy Density (HED) plasmas. In ICF experiments, high-energy x-ray radiography of an imploded core is crucial for inferring the density of the core and investigating hydrodynamic instabilities. Laser-produced characteristic Kα, in combination with a monochromatic crystal, has been applied to infer the density of fusion fuels.[38] To diagnose an implosion core compressed by Megajoule-class lasers, a high-energy broadband x-ray source (> 10 keV) is required to overcome strong self-emission from the core. Figure. 1.7 shows a typical broadband x-ray radiography experiment setup using the multi-pulse Advanced Radiography capability (ARC) backlighter at NIF. Near the peak compression, short-pulse lasers are irradiated on separate x-ray source targets to produce a broadband spectrum of x-rays. By delaying the beam arrival times, the progress of the implosion with a temporal resolution better than 100 ps can be obtained. More details of x-ray generation mechanisms will be discussed in Chapter 2.2.

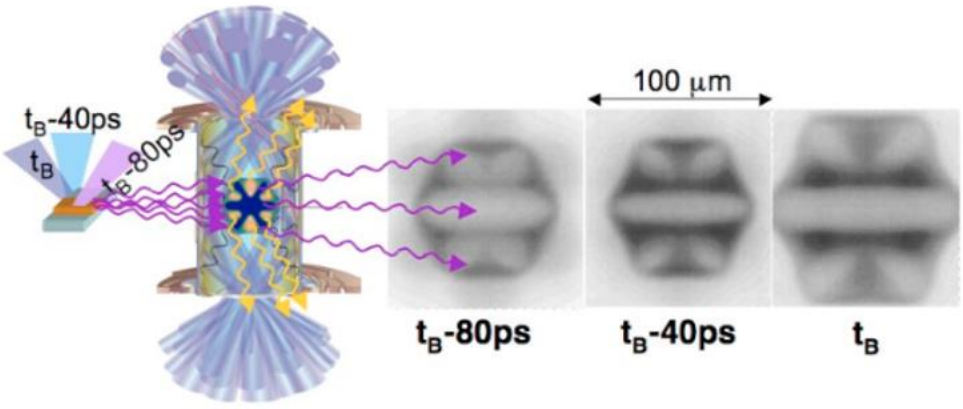

Figure 1.7 The scheme of diagnosis of ICF implosion cores and simulated images by laser-produced broadband x-ray.[39]

1.3 Thesis Overview

This thesis describes the characterization of short-pulse laser-produced fast electrons by modeling angularly resolved bremsstrahlung via 3D hybrid particle-in-cell code. Chapter 2 focuses on the physics of fast electron generation and transport in the laser-solid target interaction and the characteristics of fast electrons. Chapter 3 introduces essential numerical tools used in this work for modeling short-pulse laser and matter interaction, including Particle-in-cell (PIC) and a hybrid-PIC code Large-Scale-Plasma (LSP). Chapter 4 shows the characterization of short-pulse laser-produced fast electrons by modeling angularly resolved bremsstrahlung measurement via 3D hybrid-PIC code, together with discussions of the results. Chapter 5 performs two numerical studies using the benchmarked LSP code on a bremsstrahlung radiation source for hard x-ray radiography. Chapter 6 presents the work on designing a laser-produced x-ray source for the ZPPL experiment using the 3D hybrid modeling method. Finally, chapter 7 summarizes the results and future work.

1.4 Role of the Author

The author developed the 3D hybrid PIC modeling of angularly resolved bremsstrahlung signals shown in this thesis based on Dr. T. Daykin's 2D modeling work. The Leopard laser-solid target interaction experiments were conducted by Dr. Sawada's group. The LSP simulation input files were initially written by Dr. Sawada and later developed by the author with the help of Dr. Sawada. The author ran LSP simulations and analyzed the LSP-generated 3D x-ray photon information using MATLAB scripts, in

which the 3D photon coordinate sort and attenuation length calculation parts are independently developed by the author, and other parts are developed by the author from their 2D versions written initially by Dr. Daykin. The ZPPL experiments were carried out by Dr. Sawada's group, and the author performed and analyzed the related LSP simulations.

2. Intense Short-pulse Laser-solid Target Interaction

2.1 Generation and Transport of Fast Electrons

Fast electron generation and dynamics, including electron refluxing, are at the core of understanding high-intensity laser-plasma interaction. This field is highly relevant to fast ignition fusion and the development of x-ray, γ-ray, and other particle sources. The underlying physics of fast electron generation and transport has been studied for decades, and numerous research work has been done in physics theory, various scales of experiments, and Monte Carlo or PIC simulations. In this chapter, the generation and transport of fast electrons, which includes the absorption of laser light, the generation of fast electrons and the propagation and stopping of the fast electrons in the solid target, will be introduced.

2.1.1 Generation of Fast Electrons in Laser-solid Target Interaction

During a laser pulse interacting with a solid target, energy is transferred from the laser pulse into the plasma to produce relativistic electrons and self-generated electromagnetic fields by several absorption mechanisms: inverse bremsstrahlung, resonant absorption, Vacuum (Brunel) heating, J×B heating. These mechanisms dominate in different ranges of laser intensities under other specific conditions.

In the low laser intensity regime of 10^{12}-10^{15} W/cm^2, a collisional absorption mechanism called inverse bremsstrahlung dominates the absorption. In this process, the electrons in the laser electric field increase their kinetic energy during a collision with an ion. The laser propagates into the preplasma until the critical density, defined as $n_c =$

$1.1 \times \frac{10^{21}}{\lambda^2}$ $[cm^{-3}]$, where λ is the laser wavelength in μm. Electrons in this region oscillate in the laser-generated electric field and absorb energy from the laser. When these electrons collide with the nucleus (ions), the oscillatory energy of the electron is converted to thermal energy to heat the plasma.[40] The efficiency of the inverse bremsstrahlung is high under high-density and low-temperature conditions.

For mid-intensity laser (I~10^{14}-10^{17} W/cm^2), a collisionless absorption mechanism called resonant absorption becomes essential due to the reduction of collision frequency. When the electron density scale length is comparable to the wavelength of obliquely incident p-polarized laser light, the normal component of the electric field can resonantly drive an electron plasma wave in the direction perpendicular to the surface and accelerate electrons to the temperature of 5-50 keV.[41]

The resonance will be broken when the laser intensity ranges from 10^{16}-10^{19} W/cm^2. The ponderomotive force of the laser steepens the preplasma density gradient, pulls out the electrons into the vacuum, and then sends them back into the target plasma with the oscillation of the electric field; this process is called vacuum (Brunel) heating.[42]

When the laser intensity is as high as 10^{18} W/cm^2, a laser's strong electric and magnetic field accelerates background electrons near the critical density to above relativistic energies, which are much higher than the background thermal electrons. In this regime, fast electrons are generated predominantly by the ponderomotive potential. The fundamental physics of an electron oscillating in a non-homogeneous laser-generated electromagnetic (EM) field is explained by the derivation of the ponderomotive force in this section. The oscillating component of the ponderomotive force drives an electrostatic

field, which leads to electron heating and makes the magnetic (V×B) component in the Lorentz equation dominant. This mechanism is also called J×B force because the laser B field at relativistic intensities redirects the electron currents and accelerates electrons along the electric k-vector direction with twice the laser frequency. The laser absorption for the electrons accelerated by J×B force strongly depends on the intensity and ranges from 1-2% at $I\lambda_{\mu}$=10^{17} W/cm^2 to 10-15% at $I\lambda_{\mu}$=10^{18} W/cm^2.[43]

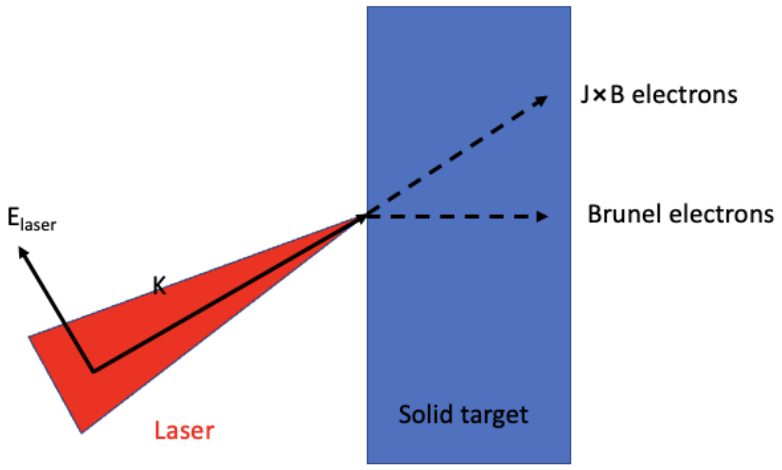

Figure 2.1 A simplified illustration of J×B and Brunel absorption mechanisms.

The ponderomotive force of an electromagnetic wave can be derived by considering an electron oscillating in a linear polarized laser with an electric field of **E** and a magnetic field of **B**. The oscillating electric and magnetic fields can be written as:

$$\mathbf{E}(\mathbf{r}, \mathrm{t}) = \mathbf{E_0}(\mathbf{r}) \cos(\omega t)\,, \tag{2.1}$$

and

$$\mathbf{B}(\mathbf{r},\mathrm{t}) = \mathbf{B_0}(\mathbf{r})\,\mathbf{c}\cos(\omega t)\,, \tag{2.2}$$

where $\mathbf{E_0}$ and $\mathbf{B_0}$ are amplitudes of electric and magnetic fields, respectively, and ω is the angular frequency. Combining Eq. (2.1) and Eq. (2.2) into the Lorentz force equation Eq. (2.3),

$$\mathbf{F} = m\frac{\boldsymbol{dv}}{\boldsymbol{dt}} = \mathrm{q}(\mathbf{E} + \mathbf{v} \times \mathbf{B}), \tag{2.3}$$

one can find the equation of motion of the single electron:

$$m\frac{\boldsymbol{dv}}{\boldsymbol{dt}} = -\mathrm{q}[\,\mathbf{E_0}(\mathbf{r})\cos(\omega t) + \mathbf{v} \times \mathbf{B_0}(\mathbf{r})\cos(\omega t)\,], \tag{2.4}$$

where m is the rest mass of an electron, and q is the electron charge. In the case of the negligible magnetic field, the second term of Eq. (2.4) can be neglected to lead to

$$m\frac{\boldsymbol{dv}^{(1)}}{\boldsymbol{dt}} = -\mathrm{q}\mathbf{E_0}(\mathbf{r})\cos(\omega t). \tag{2.5}$$

By solving (2.5) for the first-order solution of **v** (it is called the electron quiver velocity) and **r**, one can find:

$$\mathbf{v}^{(\mathbf{1})} = \frac{\boldsymbol{q}}{\boldsymbol{m\omega}}\mathbf{E_0}\sin(\omega t), \tag{2.6}$$

and

$$\mathbf{r}^{(\mathbf{1})} = \frac{\boldsymbol{q}}{\boldsymbol{m\omega^2}}\mathbf{E_0}\cos(\omega t). \tag{2.7}$$

Now, to include the effect of a small variation of the electric field and the magnetic field, i.e., the second order of Eq. (2.4), which can be written as:

$$m\frac{\boldsymbol{dv}}{\boldsymbol{dt}} = -\mathrm{q}[(\mathbf{r}^{(\mathbf{1})} \cdot \nabla)\mathbf{E_0} + \mathbf{v}^{(\mathbf{1})} \times \mathbf{B_0}]\cos(\omega t), \tag{2.8}$$

by substituting $\mathbf{r^{(1)}}$, $\mathbf{v^{(1)}}$, and the Maxwell-Faraday's equation, $\nabla \times \mathrm{E} = -\frac{\partial \mathrm{B}}{\partial t}$, into Eq. (2.8), then taking the time average over a single laser period, one can obtain

$$m\frac{\mathbf{dv}}{\boldsymbol{dt}} = \frac{\mathrm{q}^2}{\mathbf{2}m\boldsymbol{\omega}^{\mathbf{2}}}[(\mathbf{E_0}\cdot\nabla)\mathbf{E_0} + \mathbf{E_0}\times(\nabla\times\mathbf{E_0})]. \tag{2.9}$$

Using the vector identity

$$\mathbf{E_0}\times(\nabla\times\mathbf{E_0}) = \frac{1}{2}\nabla\mathbf{E_0}^{\mathbf{2}} - (\mathbf{E_0}\cdot\nabla)\mathbf{E_0}, \tag{2.10}$$

one can find the ponderomotive force,

$$\mathbf{F_p} = m\frac{\boldsymbol{dv}}{\boldsymbol{dt}} = -\frac{\mathrm{q}^2}{4m\omega^2}\vec{\boldsymbol{\nabla}}\left(\mathbf{E_0}^2(\mathbf{r})\right). \tag{2.11}$$

and it was sometimes written as:

$$\mathbf{F_p} = -\vec{\boldsymbol{\nabla}}\mathbf{U}_{\boldsymbol{p}}, \tag{2.12}$$

with $\mathbf{U}_{\boldsymbol{p}} = \frac{\mathrm{q}^2\mathbf{E_0}^2}{4m\omega^2}$. The pondermotive potential is proportional to the square of the electric field. When the laser interacts with the solid target, there will be a gradient of the electric field at the critical density region, and electrons are accelerated more by the stronger electric field region and less in the weaker field region, resulting in a net force that accelerates electron to the weaker field direction (along the laser direction).

The ponderomotive potential provides a vital scaling law for the energy of accelerating electrons called the ponderomotive scaling law (or Wilks scaling law)[44], which can be derived from

$$\mathbf{U}_{\boldsymbol{p}} = mc^2(\gamma - 1), \tag{2.13}$$

$$\gamma = \sqrt{1 + (\frac{p}{mc})^2} = \sqrt{1 + \frac{a_0^2}{2}} \approx \sqrt{1 + \frac{I\lambda^2}{1.37\times10^{18}}}, \tag{2.14}$$

Where γ is the Lorentz factor, a_0 is called the normalized vector potential of the laser's electric field, and *I* and λ are the laser intensity in the unit of W/cm^2 and wavelength in the unit of μm. It is worth noting that $a_0 = \frac{q\mathbf{E_0}}{m\boldsymbol{\omega c}}$, which comes from the maximum electron velocity ($\frac{q\mathbf{E_0}}{\boldsymbol{\omega}}$) divided by the electron rest mass (m) and the speed of light (c), is frequently used to define the intensity at which the quiver velocity of an electron becomes relativistic, i.e., the laser is in the ultra-intense regime as $a_0 \geq 1$. By using the laser intensity *I* and the wavelength λ, the heated electrons' temperature (energy) is often referred to as:

$$\mathbf{U_p} \approx \mathrm{T_{hot}} \approx mc^2 \left[\sqrt{1 + \frac{I\lambda^2}{\mathbf{1.37\times10^{18}}}} - 1\right] \approx 1\ \mathrm{MeV} \times \sqrt{\frac{I\lambda^2}{\mathbf{10^{19}}}}. \quad (2.15)$$

This scaling is essential to provide guidance on the electron energy spectrum of fast electrons for a given laser intensity and wavelength.

2.1.2 Transport of Fast Electrons in a Solid Target

Fast electron transport describes the propagation and stopping of the fast electrons in the target while they lose energy to the target by collisional, resistive, diffusive, and radiative mechanisms. A high-intensity laser pulse consists of a main peak pulse at an intensity of > 10^{18} W/cm^2 and a low-intensity pedestal. In a laser-solid interaction, the pedestal from the amplified spontaneous emission and/or low intensity (~10^{12} W/cm^2) prepulse first interacts with the target, creating a pre-formed plasma in front of the target before the main pulse arrives. Then, the interaction of the main pulse with the preplasma accelerates electrons in the preplasma to MeV energies. As shown in Figure 2.2, these energetic (fast) electrons travel mainly in the forward direction, and the collision with the

dense solid background material leads to broadening electron distribution. The forward-propagating fast electron beam leads to electron beam filamentation and generates a current-driven magnetic field, drawing a cold return current from the background electrons[45] to cancel the net magnetic field. The cancellation of the net current maintains the local charge neutrality, i.e., the net current $\vec{J}_{net} = \vec{J}_{fast} + \vec{J}_{return} \approx 0$.

The transport of a fast electron beam traversing through the target can heat the background plasma in three different mechanisms.[46] The collision of the return current with the background plasma heats the latter one with power current density $\vec{J}_{return} \cdot E \approx \eta\, j_{fast}^2$, here η is the resistivity, and it is called resistive (Ohm or Joule) heating. The heating due to direct collisions between hot and cold electrons is known as drag heating. On the other hand, diffusive heating is driven by a temperature gradient between a hot preplasma and a cold solid target.

An important phenomenon in the transport of fast electrons relevant to this thesis is sheath field generation at the target rear side (E_z in fig 2.2) and electron recirculation. A rear sheath field is generated when a fraction of the high-energy fast electrons escape from the rear surface. Strong electric sheath potential on the order of TV/m prevents the lower-energy electrons from escaping the target and forces them to recirculate within the target[47,48]. Most fast electrons traverse back and forth in the target several times if the target is thin, called refluxing or recirculation. The interplay between the sheath field and electron recirculation makes the characterization of fast electrons generated at the laser-target interaction region challenging.

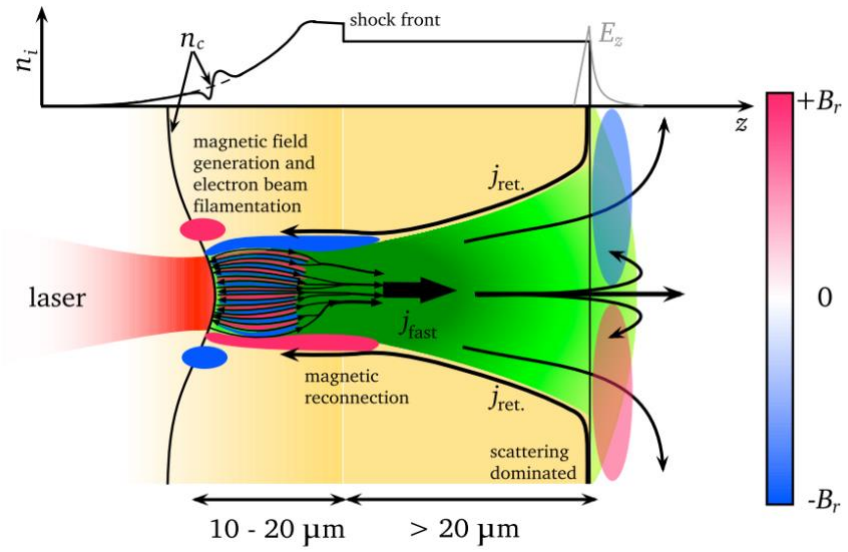

Figure 2.2 A schematic of laser-generated fast electron transport.[49]

2.2 Secondary Radiations

Two types of radiations are produced in a high-intensity laser-target interaction as laser-driven fast electrons transport through and recirculate around the target: K-shell line emission with inner shell electrons (characteristic x-rays) and continuous radiation (Bremsstrahlung) from the scattering of the electrons by target ions.

2.2.1 Characteristic Radiation

Characteristic line emissions are produced when an excited electron fills a K-shell vacancy created by an energetic electron or photon colliding with target atoms. Each element has a specific number of orbits, and each orbit can hold up to a maximum number of electrons. In the present context, as shown in Figure 2.3, a fast electron with a higher

kinetic energy than the K-shell binding energy can knock out electrons in the K-shell orbit and leaves a vacancy. The vacancy is quickly filled by an excited electron from a higher orbit, and a photon with an energy equal to the difference in the transition energy of the two levels is produced. For example, if a K-shell electron is lost due to collision, and one of the L-shell electrons fills the vacancy, producing the radiation called the Kα emission. The photon energy of the characteristic x-rays (e.g., Kα and Kβ) depends on the target element, so it is broadly used for industrial applications, such as material analysis, non-destructive testing, and radiation therapy, as well as for HED science applications, including flash Kα radiography of an ICF implosion core.

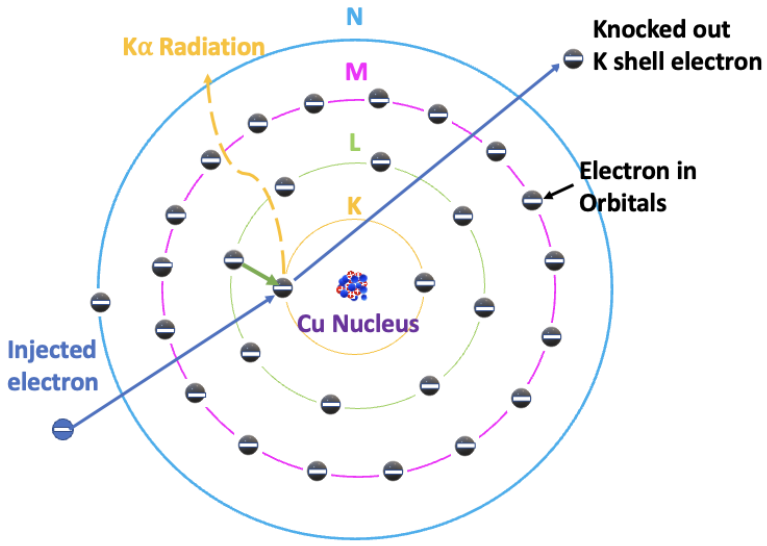

Figure 2.3 A schematic of the generation of characteristic radiation.

2.2.2 Bremsstrahlung Radiation

Bremsstrahlung is a German word for braking radiation, which is generated from the process of energetic electrons losing energy during the interaction with the positive nucleus within an atom. Bremsstrahlung radiation is a critical source of energy loss for relativistic electrons via collisions and deflections. Since an electron may lose any portion of its energy during the interaction with the atom, bremsstrahlung radiation becomes a continuous broadband spectrum ranging from zero to the maximum kinetic energy of the energetic electron. Such a broadband hard x-ray bremsstrahlung radiation is preferred in diagnosing a fusion core and radiographing a high-areal density object to overcome strong self-emission or its high areal density.

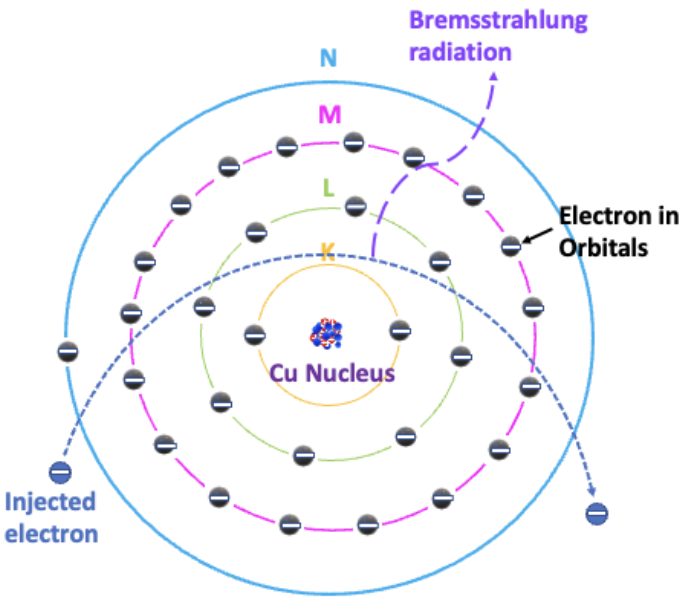

Figure 2.4 A schematic of the generation of bremsstrahlung radiation.

2.3 Characteristics of Laser-driven Fast Electrons

Laser-produced fast electrons can be characterized by three key parameters: electron energy distribution, laser-to-electron energy conversion efficiency, and electron beam divergence angle. To infer all three electron characteristics, multiple experimental measurements are required, such as a magnet-based electron spectral measurement[50,51], Kα fluorescence measurement[52], bremsstrahlung photon measurement[53], optical probing[54], thermal imaging[33,55], coherent transition radiation (CTR)[Error! Bookmark not defined.,Error! Bookmark not defined.], incoherent transition radiation (ITR)[47] and nuclear activation[56,57]. This subchapter introduces these three parameters as well as experimentally and numerically inferred parameter values from previous studies.

2.3.1 Electron Energy Distribution

The kinetic energy of a laser-driven fast electron is often estimated using the ponderomotive potential, as described in Chapter 2.1. Because of the temporal and spatial variations in laser intensity, the electrons generated have a broad energy spectrum. PIC simulations indicate that laser-driven fast electrons are a monotonically decreasing spectrum, but it does not follow a simple theoretical function. Thus, the energy estimated using the ponderomotive potential is often referred to as the mean energy of the fast electron energy spectrum. In particle-transport simulations, the continuous electron distribution function (dN/dE) is often simplified using a Maxwellian, Boltzmann distribution function or a sum of multiple exponential energy distributions, such as $e^{-(k_e/T_1)}+e^{-(k_e/T_2)} + e^{-(k_e/T_3)}+\cdots$, where k_e is the kinetic energy of the electron and T_1,

T_2, T_3… are a slope temperature of each spectrum. In the high-intensity laser-target interaction, the laser-driven fast electrons are a non-thermal component of the electron energy distribution, often described as a hot component with a single slope temperature, T_h.

The accurate characterization of the electron distribution in measuring escaped electrons is difficult since only the high energy tail of the electron spectrum can escape from the target rear due to the sheath potential. To infer the electron distribution at the generation point, indirect measurements that have been used include the interpretation of measured bremsstrahlung radiation and ion acceleration. By combing experimental measurements and analytical modeling, a few scaling laws were developed to estimate the electron temperature, such as two often used scaling laws: the ponderomotive scaling law by Wilks et al.[44] and the Beg scaling law[58]. Even though scaling laws are indeed beneficial as references to infer electron temperature, detailed PIC simulations show that the energy distribution is often more complex than simple scaling laws.

2.3.2 Electron Divergence Angle

Characterization of the electron beam divergence angle is essential for applications such as Fast ignition since a less divergent angle of fast electrons is preferred to deposit their energy in the core. However, the characterization of the divergence angle of fast electrons is complicated. The angular distribution of fast electrons depends on various parameters, such as the laser energy, pulse duration, spot size, laser intensity, and target parameters. During the transport of fast electrons in a solid target, electrons experience

strong scattering and self-generated resistive fields inside the solid target. The spread angle of the electrons is thus greatly altered from the initial injection position. In particular, the high resistivity in the metal target could generate a resistive collimation effect, which reduces the divergence of the electron beam. For example, an initial electron divergence half angle of 50° is assumed in a hybrid simulation[59] to reproduce a full propagation angle of 35° in experiment[60]. The direct measurement of the divergence angle of the injected electron beam is almost impossible, so alternative diagnostic techniques have been developed.

In the past few decades, numerous experimental works on fast electron divergence measurements have been conducted using CTR[61,62], ITR[47], and Kα emission[33,34]. The divergence half angle estimated from the Kα measurements ranges from 20 to 50°, and CTR and ITR measurements indicate less than 20° divergence half angles. For instance, Green et al.60 and Armstrong et al.[63] measured 0-35° divergence angles using Kα emission measurements of 25-100 μm Ti or Cu targets for laser conditions of 1μm wavelength, 2-5 ps duration, and intensity 10^{17} to 10^{21} W/cm^2. These measured divergence angles were obtained under the assumption that the electron divergence is given by the effective propagation angle measured from experiments, so if the resistivity in the solid target is taken into account, the initial fast electron divergence should be higher than these measured angles. On the other hand, simulations[59,64] indicate the divergence half-angle could be large as 50°-55°, or sometimes even larger. The significant variation may be due to the limitation of the measurement method, such as Kα fluorescence measurement, in which the magnetic field generated at the interface with the buried layer may limit the electron transport at high

laser intensity and distort the measurement result[65]. Meanwhile, as shown in Figure 2.2, different laser conditions, target material, and beyond-controlled pre-plasma profiles before the front surface of the target are all possible factors that need to be considered. In conclusion, a complete understanding of the fast electron divergence angle is challenging and has to include multiple factors such as the laser condition, target size, measurement method, etc.

2.3.3 Electron Beam Energy and Laser-to-electron conversion efficiency

The energy conversion efficiency from the laser to fast electrons (and furthermore to the target and the x-ray radiation generated from the target) is of significant importance to many relevant applications. The conversion efficiency can be inferred by modeling the bremsstrahlung x-ray and/or Kα emission measurements. Numerous experiments and calculations exist on the conversion efficiency η_{L-e}. For example, Scott et al.[66] found laser energy absorbed into forward-going fast electrons to be 16 ± 4% for frequency doubled light at a peak laser intensity of 9×10^{18} W/cm^2; Nilson et al.[67] found 10-30% η_{L-e} for various volume target irradiated by 1 ps/10 ps, 1-1000 J laser with intensity larger than 10^{18} W/cm^2, and Chen et al.[31] found η_{L-e} to be ~20-40% for laser averaged intensity from 3×10^{18} W/cm2 to 8×10^{18} W/cm^2, while Westover et al.[68] used Monte Carlo modeling and hybrid-transport modeling to obtain 30% and 34% laser to fast electron conversion efficiency, respectively, for laser with a peak intensity of 2×10^{20} W/cm^2. It is worth noting that although these parameters have been widely investigated, a simultaneous determination of fast electron characteristics is challenging because of limitations in

different diagnostic techniques and numerical methods. This thesis work was to develop a new approach to overcome these issues, and details are presented in Chapter 4.

2.4 Diagnostics of Fast Electron Characteristics

In this thesis work, a magnet-based electron spectrometer and filter stack bremsstrahlung spectrometers were used. This subchapter presents the concept of each diagnostic, example measurements, and data analyses.

2.4.1 Magnet-based Electron Spectrometer

A magnet-based electron spectrometer[51] directly measures the high energy (above 1 MeV) electrons that escaped from the target rear along the laser axis. Figure 2.5 (a) is a schematic of an electron spectrometer and an example of scanned data from the Fuji Biological Analysis System (BAS) MS-type Image Plate (IP), which was used for both the electron and bremsstrahlung spectrometers. Electrons entering a $1mm^2$ opening of the spectrometer are bent by the magnetic field and dispersed along the image plate. The electrons' deposition positions are determined by the magnet's strength, the lower energy electrons are deposited near the entrance, and the high energy ones can travel further to the right of the IP in the image. In a Leopard laser experiment, the spectrometer was placed at 27.4 cm from the target chamber center (tcc) along the laser forward direction.

Information on the recorded electron energy spectrum is retrieved by scanning the IP with an FLA-5000 scanner and converted to digital signals with the unit of Photo Stimulated Luminescence (PSL)[69]. Figure 2.5(b) shows a lineout of the digitized IP signals

with a single slope temperature fitting. The calibration of the signal intensity to the number of electrons and the electron dispersion was established in a separate experiment on the TITAN laser at Jupiter Laser Facility [70]. The slope of a measured escaping electron spectrum primarily depends on a peak laser intensity since the measurement is a fraction of high-energy electrons of the spectrum generated. Other factors, such as the preplasma scale length and target position, can affect the electron spectrum. However, the slope of the electron spectrum can be used to monitor the shot-to-shot variation in experiments. The measurements of laser-driven fast electrons in Leopard laser experiments are discussed in Chapter 4.

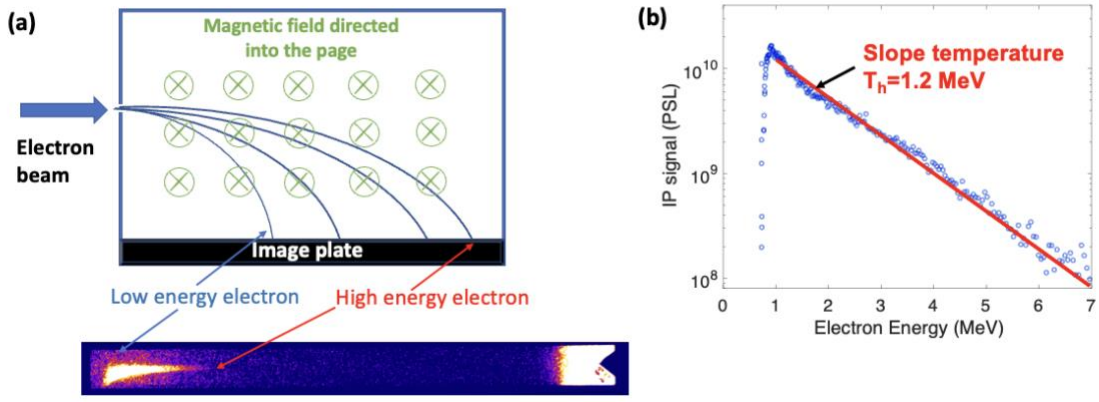

Figure 2.5 (a) A schematic of the magnetic-based electron spectrometer and an example of a scanned IP image. (b) An example lineout of a measured electron spectrum with a single slope temperature fit in the unit of PSL.

2.4.2 Filter Stack Bremsstrahlung Spectrometer

A filter-stack spectrometer has been used to measure a broadband hard x-ray spectrum.[53] The bremsstrahlung spectrometer used in this work consists of differential metal filters and IPs. Bremsstrahlung signals are recorded on each IP behind 15 layers of filter made by different materials from low Z to high Z materials. The details of the filter material, thickness, and minimal photon energy required to transmit through the filter are listed in Table 1. The minimum photon energy required to penetrate through each filter increases with the layer number from ~13 to 550 keV. This particular spectrometer has a photon range between 10 and 800 keV and has been absolutely calibrated.

Table 1. Filter stack bremsstrahlung spectrometer's filter material, thickness, and minimal energy required to deposit energy into the corresponding IP.

Layer	Material	Thickness	Min energy
0	Teflon	5 mm	12.91 keV
1	Al	100 μm	13.21 keV
2	Ti	100 μm	14.83 keV
3	Fe	100 μm	19.33 keV
4	Cu	100 μm	25.2 keV
5	Mo	150 μm	32.47 keV
6	Ag	500 μm	42.82 keV
7	Sn	500 μm	59.12 keV
8	Ta	1.58 mm	104 keV

9	Au	1.143 mm	189.35 keV
10	Pb	2.272 mm	217.43 keV
11	Pb	3.372 mm	270.66 keV
12	Pb	4.473 mm	310.8 keV
13	Pb	4.473 mm	378 keV
14	Pb	4.473 mm	439.2 keV
15	Pb	4.473 mm	550 keV

Figure 2.6(a) shows a schematic of the bremsstrahlung spectrometer, an example of scanned IP raw signals, and the analyzed signals. The filters and IPs are placed in a 6 mm thick Lexan cartridge housed by a 1.8 mm thick lead enclosure. Each IP is sandwiched by 250 μm Mylar sheets. A magnet is placed before the spectrometer to deflect energetic charged particles to avoid unwanted noise. A lead collimator, also placed in front of the spectrometer, has a 0.5-inch diameter round opening to limit the field of view to the housing. In Fig 2.6(b), an example of the signals on IPs is for x-rays from shallower layers to deeper layers in the spectrometer from left to right. The raw measured signals are subsequently analyzed by using Image J. Three oval regions are chosen in each circle of the signal, and the measured values in each region are averaged and recorded as the signal, while the standard deviation of the measurement and the gradient of the cannon signal (the difference between the three regions) are recorded for each layer.

Figure 2.6(c) shows raw bremsstrahlung spectral signals recorded for a 100 μm thick Copper target backed by a plastic. The unit of the signals (Y axis) is PSL/pixel^2, and

the x-axis is the IP layer number from 1st to 15th. The error bar of a signal is calculated from the quadrature addition of three factors: the standard deviation of the measurement, the gradient of the cannon signal, and a 3% scanner response variation from the IP. The signal strength depends on the position of the spectrometer and the input electron parameters.

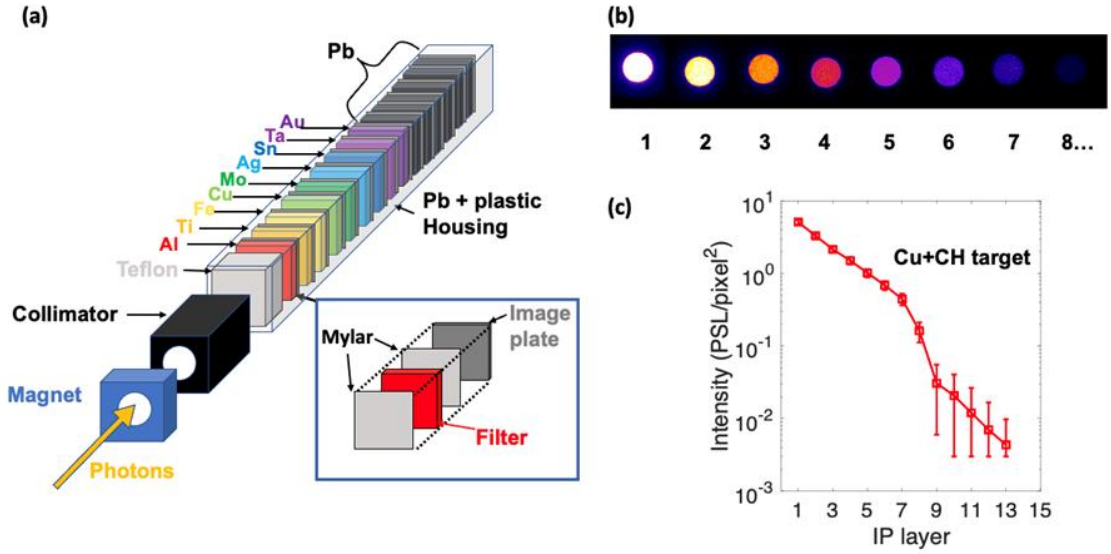

Figure 2.6 (a) Schematic of a differential filter stack bremsstrahlung spectrometer and an example of recorded signals on IP. (b) An example of the measured raw bremsstrahlung signals on IPs. (c) Analyzed bremsstrahlung signals from a 100 μm Cu target with CH backing irradiated by the Leopard laser.

The bremsstrahlung spectrometer has been used to characterize short-pulse laser-produced fast electrons in combination with numerical modeling. Since its development in 2009, Chen et al.[31] and Westover et al.[71] used one bremsstrahlung spectrometer to deduce

conversion efficiency ranges and slope temperatures with an assumed divergence angle by modeling the data with Monte Carlo simulations. Later, Chen et al. [72] used three bremsstrahlung spectrometers to compare the measurements with 2D multi-stage simulations to further constrain fast electron characteristics on TITAN. To infer the conversion efficiency, the modeling for the above work was performed in a 2D cylindrical geometry. More recently, Sawada[73,74]and Daykin[75] used two bremsstrahlung spectrometers together with a 2D Cartesian geometry to incorporate the injection axis of an electron beam mimicking the laser incident angle. A better agreement between the measurement and the 2D Cartesian modeling was obtained. However, the conversion efficiency cannot be characterized by using these 2D simulations. To overcome this issue, a hybrid PIC code is used in a 3D Cartesian geometry to model bremsstrahlung measurements at two angular positions. A unique set of all three fast electron parameters have been inferred by combining results of refluxing and non-refluxing targets, as shown in Chapter 4.

3. Numerical Modeling of Short-pulse Laser and Solid Interaction

3.1 Particle-in-cell (PIC) and Hybrid-PIC Simulation

Plasma simulations can be categorized into three approaches: a single-particle, kinetic or fluid calculation. To compute the interaction of laser light with plasma and the generation of fast electrons, a particle-in-cell (PIC) code[76] is a suitable tool, which solves Maxwell's equations with a "macroparticle" to represent many real particles with the same property. In a PIC calculation, these macroparticles are set to have the same charge-to-mass ratio to mimic the behavior of a real particle in the electromagnetic field of the laser. Another important feature of the PIC method is that it can follow the trajectories of charged particles in self-consistent electromagnetic fields. Figure 3.1 shows a typical calculation step in a PIC code. A PIC calculation proceeds in the following steps. By giving initial positions and velocities, the code calculates the charge densities of plasma at each grid point using weighted position and velocity. Then, the electric and magnetic fields on the grid are updated by solving Maxwell's equations. In the third step, the force exerted on the particles is calculated using the weighted fields at each grid point. Finally, by integrating the equation of motion, a new particle position and velocity are calculated for the next circle.

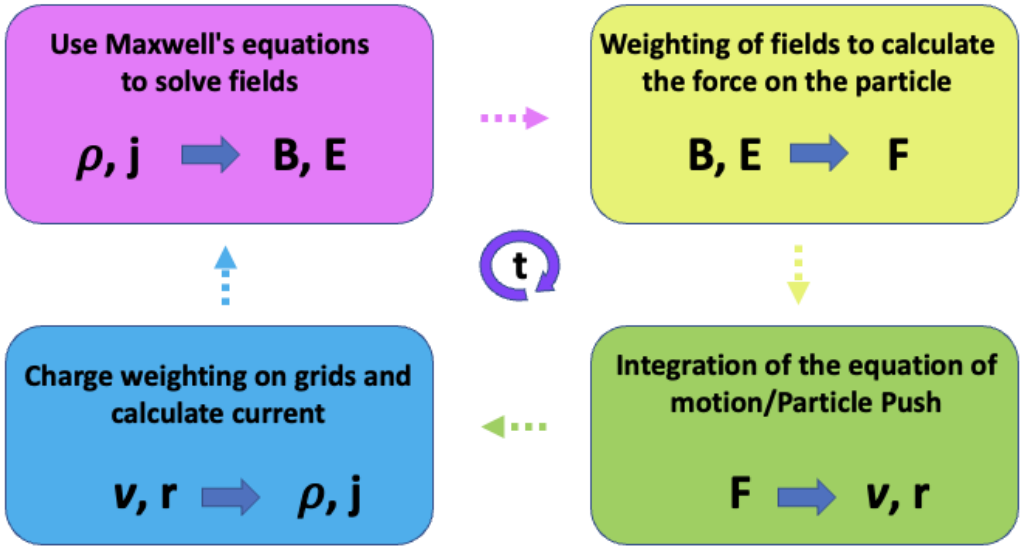

Figure 3.1 A schematic of the PIC simulation method.

PIC codes can run in an explicit or implicit method. The PIC simulation cycle shown in Fig. 3.1 is an explicit scheme where the equations of motion for the particles and the electromagnetic fields are solved explicitly in time. In this approach, the grid cell size and a time step of a calculation are required to be set much smaller than the Debye length due to numerical instabilities, particularly at high particle densities or in highly dynamic plasma environments. In contrast, the implicit method does not depend on the spatial and temporal constraints for a stable operation. It makes a suitable guess for the future time step with a predictive algorithm, and a current time step is calculated from that prediction, so the implicit equation must be solved iteratively due to the unknown quantities for the current and future steps.

Since the explicit PIC scheme requires fine spatiotemporal grids to resolve the laser wavelength, PIC simulations are typically limited to a much smaller simulation space and time than a target and laser duration used in an experiment. Numerical studies of laser-driven fast electron production and transport have been performed in two steps: first, a relatively small-sized (a few μm) PIC simulation is performed to calculate the generation of fast electrons, and then, the propagation of the fast electrons is modeled using a hybrid or implicit PIC code in a much larger space (a few hundred μm or larger) and longer time.

A hybrid PIC code, a code extensively used in the thesis work, uses a similar kinetic description to model the transport of charged particles, but different from PIC codes, it can simulate the fast electron transport physics on an experimental scale by injecting fast electrons instead of resolving grids for the laser-plasma interaction. Both PIC and hybrid PIC methods use "macroparticle" for thousands of the same species of particles to save computation time by calculating particle interaction between each macroparticle instead of an individual particle. The time step in this part is calculated by the courant limit, $\Delta t = \Delta x/c$, where Δx is the cell size, and c is the speed of light. If the courant limit exceeds 1, the time step is too large to see the particle in one cell, so it needs to be less than 1 so the light cannot travel more than one cell in one step. The fluid approach in the hybrid PIC code treats background plasma as a quasi-neutral fluid, in which the moments of background fluid are collected and interpolated onto the grid, and simplified Maxwell equations are used to solve the field. This fluid treatment does lose some physics, such as the inertia of charged particles and complex kinetic effects, but it saves much computational time by using macroscopic quantities for the background plasma. As

mentioned, the hybrid PIC method is usually applied to the second step of the fast electron simulation. For example, in this work, a fast electron beam, instead of a laser, is injected into the solid target, and a Monte Carlo code is used to simulate the scattering and transport of electrons inside the target, along with the calculation of self-generated fields.

3.2 A Hybrid PIC Code: Large Scale Plasma (LSP)

A hybrid PIC code, Large Scale Plasma (LSP)[77,78], is used to simulate the transport of fast electrons in plasmas, including the development of fields self-consistently in this work. LSP is capable of running 1D, 2D, and 3D simulations in cartesian, cylindrical, and spherical geometry for large-scale plasmas. It has a hybrid mode, as well as several types of electromagnetic field solutions: the standard (explicit) leapfrog algorithm and direct-implicit algorithms using iterative alternate-direction implicit (ADI), a two-step ADI, and matrix inversion. In addition, several options for advancing particles are included in LSP: the standard momentum-conserving and energy-conserving PIC algorithms, cloud-in-cell (CIC) algorithm, and direct-implicit algorithm, which can be used in either the PIC or CIC model. The LSP code takes into account the stopping power with the continuous-slowing-down approximation (CSDA) range as well as scattering and radiative loss for the electron transport processes. The generation of bremsstrahlung and Kα photons in LSP is modeled using a cross-section calculated with the Integrated Tiger Series (ITS) code. Magnetic fields generated by resistive gradients or filamentation are not included in LSP.

Numerous studies of the production and transport of fast electrons or proton beams have been performed using the LSP codes[79,80] in the past two decades. For instance, Welch

et al. [80] compared 2D fully kinetic simulations with the results using LSP in 3D cylindrical coordinates by simulating the propagation of the circularly polarized laser light in a thin metal foil and the transport of electrons and protons, and it is found that 3D simulation is necessary to quantify the beam transport. Daykin et al.[75] used 2D LSP simulations to show the benchmarking of the electron stopping and scattering as well as the angular distribution of bremsstrahlung generated in solid Cu against a Monte Carlo code Electron Gamma Shower 5 (EGS5) [81] incorporated in Particle and Heavy Ion Transport code System (PHITS)[82].

3.3 3D Hybrid-PIC LSP Simulations for Angularly Resolved Bremsstrahlung Radiation

This subchapter presents the procedures of angularly resolved bremsstrahlung calculations using the LSP code in a 3D Cartesian coordinate. The calculations were performed in an implicit method by injecting a beam of fast electrons. Key information required in an input file is on the initial simulation geometry, target dimensions, and electron pulse duration, in addition to the injected fast electron beam parameters. A fast electron energy spectrum is represented by an exponential function with a single slope temperature (T_h). In addition, an electron beam divergence half angle (θ) using a Gaussian distribution and the total injected electron beam energy (E_b), which changes the total electron number, are defined. These three parameters are the main variables to compute bremsstrahlung and synthetic bremsstrahlung spectrometer signals.

In this work, using a 3D simulation coordinate is essential for accurately simulating the development of self-consistent fields at all target-vacuum boundaries and the recirculation of fast electrons. Figure 3.2(a) shows a schematic of a 3D LSP simulation setup for a solid Cu foil attached to a plastic foil. The simulation space has a 2.0×1.5×2.0 mm^3 volume with a 10 μm cell in each direction. A 100 μm thick Cu foil with a surface area of 1.0 mm^2 is placed at the center of the space. In the Leopard experiment shown later, bremsstrahlung radiation was measured from a bare Cu foil and a Cu foil with a CH backing. The dimension of the CH backing was a 6.35 mm radius hemisphere with a height of several centimeters. In the LSP simulation, it is limited to the one with 650 μm in thickness and 2.0×2.0 mm^2 in surface area that fills the rear side of the simulation space. The addition of the CH backing to the rear side of the Cu layer prevents the sheath field development, reducing the recirculation of fast electrons and, subsequently, the generation of bremsstrahlung radiation. The size of the CH backing is varied to study its effectiveness for mitigating electron recirculation and is presented in Chapter 5. The simulation uses the complex frequency shifted perfectly matched layer (CFSPML) as a boundary condition. This layer allows modeling freespace boundary conditions imposed on fields and particles, so the plastic backing acts as an infinite layer.

A beam of fast electrons with a 20 μm radius spot is injected at the first cell of the Cu foil in the +Y direction with a given set of electron parameters (T_h, θ, and E_b). The incident angle of the beam is 30° from the target normal in the equatorial plane. The pulse duration of the electron beam is assumed to be a Gaussian profile with 0.35 ps FWHM and its peak at 1.2 ps. The pulse profile is shown in Fig. 3.2 (b). Most simulations run up to

~20 ps. For the x-ray generation in Cu and CH, LSP uses a pre-computed cross-section file by the ITS Monte Carlo code. It also uses an equation of state and an opacity table for Cu calculated by Prism Opacity and Equation of State code (PROPACEOS). Simulations were performed using the group's Argo cluster.

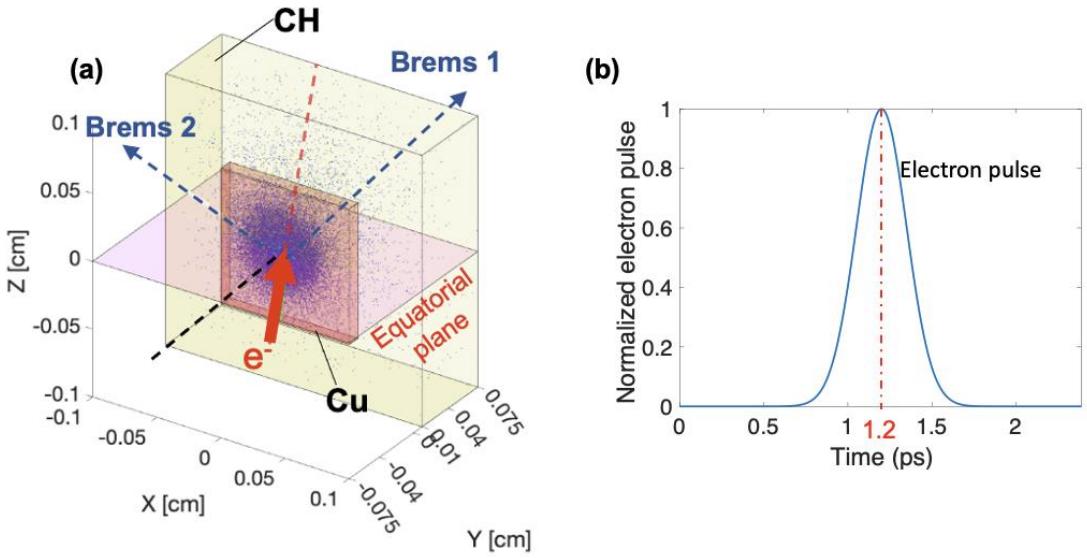

Figure 3.2 (a) A schematic of the 3D simulation of a Cu-CH target, and (b) The pulse profile of the injected fast electron beam.

Simulation results include the evolution of fast electron propagation, electric and magnetic field development, and x-ray photon generation. Information on photons, including characteristic x-rays and continuous bremsstrahlung radiation, in a position and momentum space is exported in text files at a time interval of 0.25 ps. Then, MATLAB scripts are used to post-process the data of photon charges, energies, positions, and

velocities for calculating the transport of the photons through the target. The photons that escaped from the target are sorted into a spherical space divided by a polar angle *theta* (angle with respect to the polar axis) and an azimuthal angle *phi* (angle of rotation from the initial meridian plane). In each spherical segment, the photons are sorted into 150 energy spectral bins logarithmically spaced between 1 keV and 100 MeV. Finally, together with a time interval, the number of photons is stored in a four-dimensional function [f (Energy, *theta, phi,* time)] for the photon energy, the polar and azimuthal angles. To investigate angular-dependent bremsstrahlung radiation recorded by bremsstrahlung spectrometers in the equatorial plane, the function is integrated over the polar angle near the plane, and azimuthally resolved x-ray spectra are calculated to compare with experiments. Figure 3.3 shows calculated broadband spectra with and without x-ray attenuation by the target in the target's normal direction. Since the birth location and velocities are known, the attenuation length and transmission are calculated for each photon through the target using the x-ray mass attenuation coefficients[83] of each target element. As shown in Fig. 3.3, the majority of x-ray attenuation by a 100 μm copper target is below 100 keV, and there is almost no attenuation for higher energy photons.

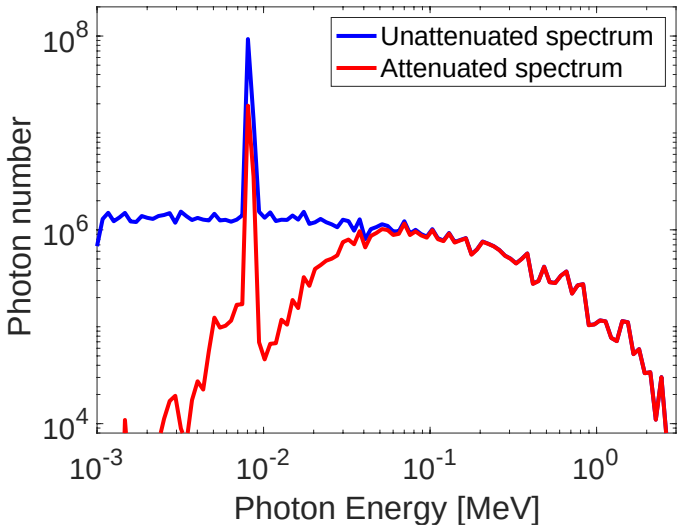

Figure 3.3 Unattenuated and attenuated photon spectra of a 100 μm Cu target with T_h=1.0 MeV, θ=70°, and E_b=1.5 J.

A calculated bremsstrahlung spectrum is obtained by averaging over ±20° in the direction of interest and is converted to a spectrometer signal using a bremsstrahlung spectrometer response matrix (SRM)[53]. SRM results from Monte Carlo simulations for the minimum energy required to be deposited in each IP layer. Figure 3.4(a) shows the spectrometer response matrix for the detector used. The matrix contains 15×150 elements corresponding to the 15 layers of IPs of the bremsstrahlung spectrometer and the 150 energy bins in the photon spectrum. Applying SRM to a calculated x-ray spectrum yields a dose signal as a function of the IP layer in the unit of MeV/cm^2. Figures 3.4(b) and 3.4(c) show an example of simulated x-ray spectra at 22° and 40° from the laser injection direction and corresponding doses calculated using SRM, respectively. The conversion from the x-

ray spectra to the spectrometer signals allows for directly comparing the simulation results to measurements.

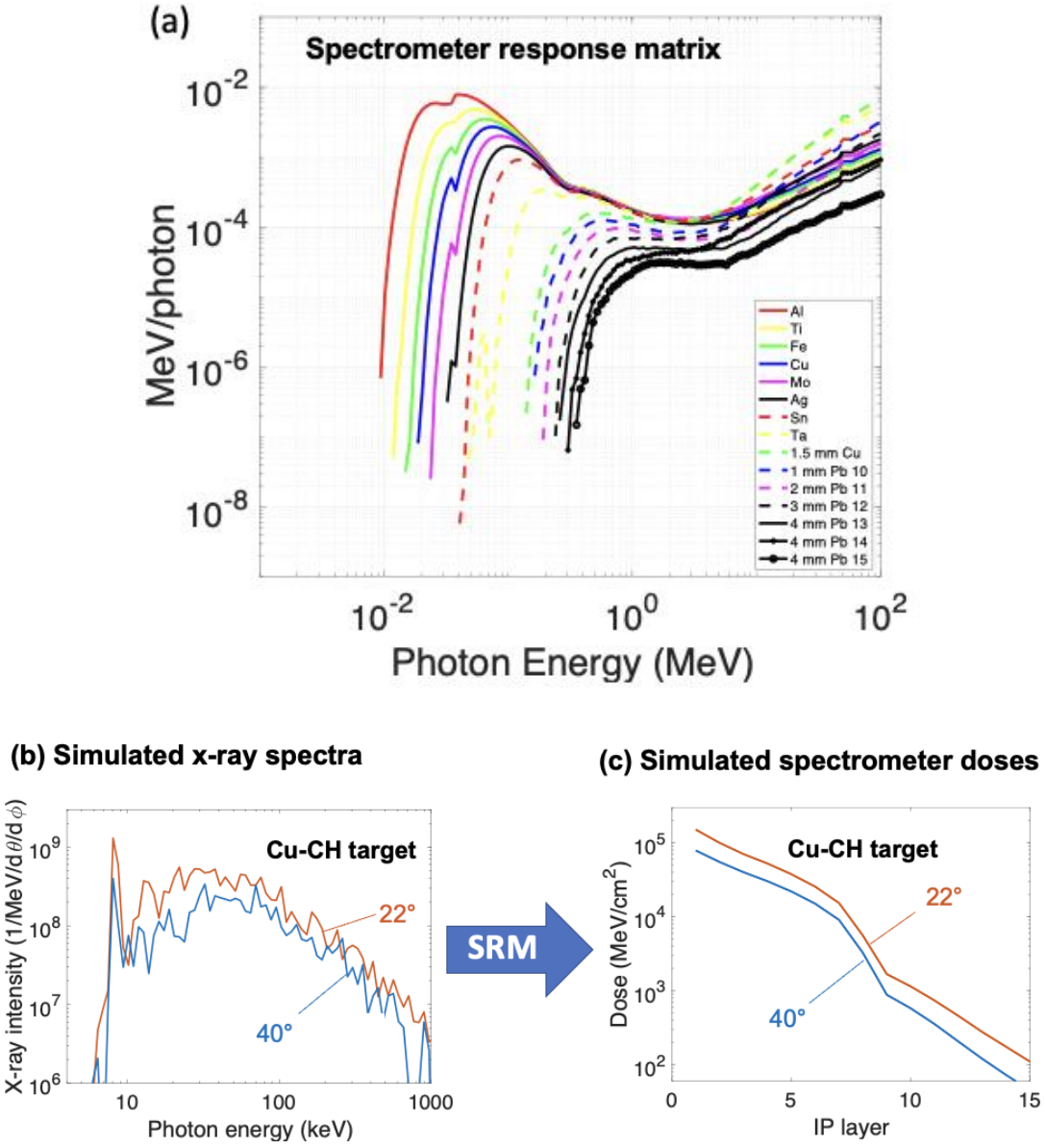

Figure 3.4 (a) The spectrometer response matrix for the bremsstrahlung spectrometer used in the Leopard experiment. (b) LSP simulated x-ray spectra of a Cu-CH target with T_h=1.0

MeV, θ=50°, and E_b=1.5 J. (c) Converted spectrometer signals by multiplying the SRM by the LSP simulated x-ray spectra.

One of the major differences between a hybrid PIC and a Monte Carlo code is the self-consistent field generation associated with electron transport. The strength of electric and magnetic fields depends on the number of escaping electrons from the target. Since the fast electrons traverse within the foil near the speed of light, the interplay between the spatial structure of the fields and electron trajectories changes quickly. Here, using an electron tracking feature in LSP, the time evolution of the electric and magnetic fields, as well as the trajectories of fast electrons, is presented. A simulation shown here uses the electron parameters of T_h = 1.0 MeV, θ = 50°, and beam energy, E_b = 1.1 J. Figure 3.5(a) shows a snapshot of the total electric field in the Y-Z plane (X=0) at 4 ps. The magnitude of the peak electric fields generated around the Cu foil exceeds 10 TV/m. Figures 3.5(b)~ 3.5 (d) show the trajectories of 0.4, 1.0, and 5.0 MeV electrons for simulation times up to 5 ps. The 0.4-MeV electrons are collisionally stopped within the Cu foil. Most of the 1-MeV electrons are affected by the front and rear sheath fields, forcing the electrons to propagate to the edge of the foil. These electrons propagate on the target surface toward the foil edges rather than penetrate back into the target. As a result, strong sheath fields are also established near the Cu edges at Z=±0.05 cm, as in Fig. 3.5(a). The majority of the 5-MeV electrons escape from the target rear. The color of the trajectories indicates the timing of the electron injection. Some of the 5 MeV electrons injected at the peak of the pulse (orange lines) are largely deflected and pulled back by the fields to the corner of the foil.

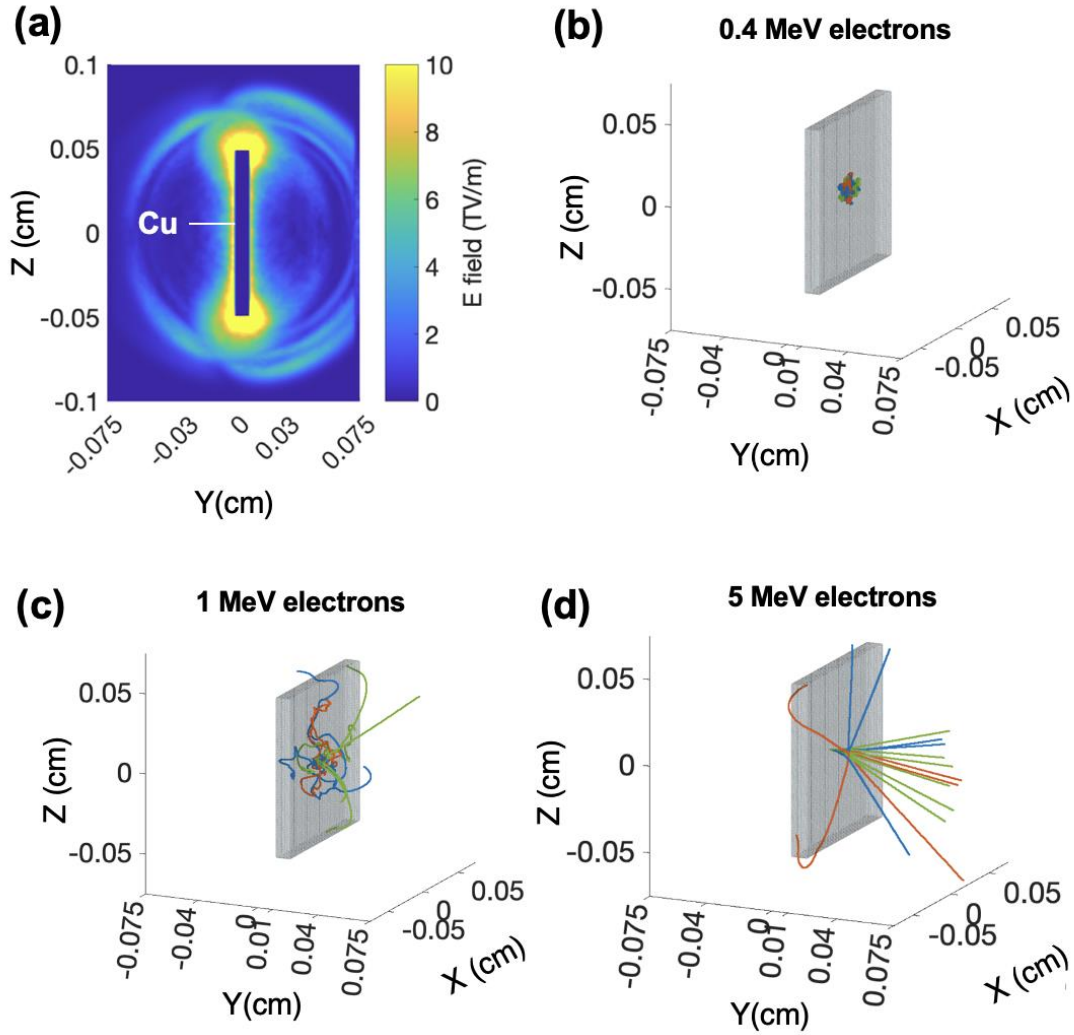

Figure 3.5 (a) A map of the total electric field in the Y-Z plane (X=0) at 4 ps. The trajectories of electrons with the kinetic energy of (b) 0.4 MeV, (c) 1.0 MeV, and (f) 5 MeV.

These simulations demonstrate that: (1) The non-normal electron injection produces an asymmetric electron beam distribution with respect to the target normal, affecting the resulting bremsstrahlung angular distribution to be also asymmetric. (2)

Bremsstrahlung radiation generated from electron recirculation is dominated by electrons with energies less than ~5 MeV. (3) Electrons trapped by the rear sheath field are deflected sideways rather than forced to execute simple back-and-forth motion within the foil.

Figures 3.6(a) and 3.6(b) show simulation results with various slope temperatures and electron beam energies, respectively. In the simulations, only one electron parameter is varied to study the changes in spectrometer doses. In particular, Fig. 3.6(a) shows that the increase in slope temperature makes a spectrum of the dose signal flatter when the beam energy and divergence angle are fixed. Meanwhile, as shown in Fig. 3.6 (b), the dose signal monotonically increases as the input electron energy increases when the slope temperature and divergence angle are fixed. The dependence of a dose spectrum on the divergence angle varies with the target type and in different diagnostic directions, and details will be discussed in Chapter 4.

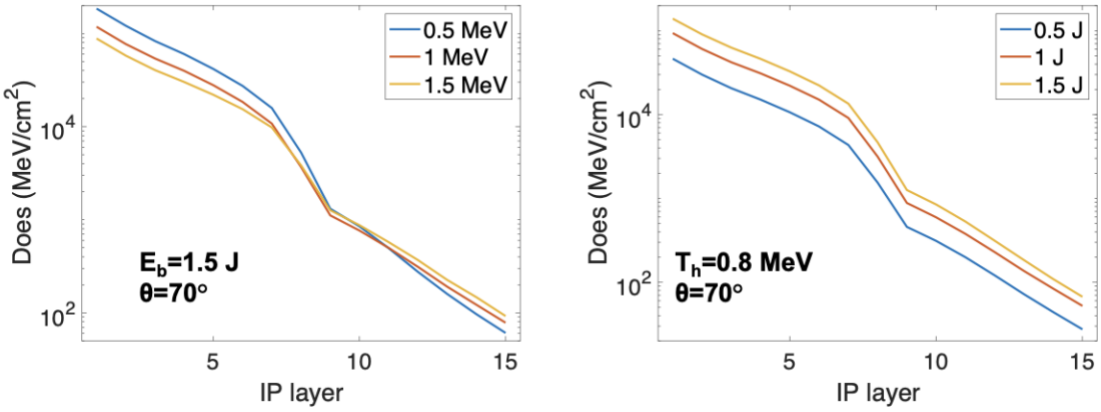

Figure 3.6 Calculated bremsstrahlung signals (a) with different T_h and (b) with different beam energies E_b. The divergence angle is fixed at 70°.

4. Characterization of Short-pulse Laser-produced Fast Electrons by 3D Hybrid Particle-in-cell Modeling of Bremsstrahlung

Modeling of bremsstrahlung measurements with a PIC, Monte Carlo, or hybrid PIC code has been used to provide insights into the fast electron characteristics of the electron slope temperature, divergence angle, and laser-to-electron conversion efficiency. However, previous works using 2D cartesian or cylindrical simulations can only infer one or two fast electron parameters partially due to an unclosed geometry for energy conservation in the 2D cartesian or the inaccurate electron recirculation calculation in the 2D axisymmetric geometry. This chapter presents a hybrid PIC modeling in a 3D cartesian coordinate to characterize short-pulse laser-produced fast electrons by modeling angularly resolved bremsstrahlung measurements. Subchapter 4.1 first introduces experimental measurements with two filter stack bremsstrahlung spectrometers and an electron spectrometer in a Leopard laser experiment. Then, Subchapters 4.2 and 4.3 present 3D LSP simulations and fitting results to determine the fast electron parameters, respectively. Subchapter 4.4 summarizes this chapter of the work. The work presented in Chapters 4 and 5 has been published in a peer-reviewed journal, Physics of Plasmas [L. Chen and H. Sawada, Phys. Plasmas **29**, 93104 (2022)].

4.1 A Leopard Laser Experiment for Bremsstrahlung Measurements

An experiment using the Leopard short-pulse laser was carried out to measure angularly resolved bremsstrahlung radiation. Figure 4.1 shows a schematic of the Leopard laser experiment. In this experiment, the laser produced a pulse with 15 J energy in 350 fs-long pulses (FWHM) at a wavelength of 1057 nm. The beam was focused tightly with an f/1.5 dielectric-coated off-axis parabolic mirror onto the target at an incident angle of 30° with an S-polarization. Measurement of the beam energy in the target plane showed that 30% of the laser energy was contained within an ~8 μm diameter spot[84]. The on-target peak laser intensity was estimated to be $\sim 2\times10^{19}$ W/cm^2. Bremsstrahlung photons generated during the electron transport were recorded using two calibrated differential filter stack spectrometers at +22° and -40° from the laser axis, counterclockwise and clockwise, respectively. In addition, a magnetic-based electron spectrometer is fielded along the laser direction to measure the number of escaped electrons from the target rear.

The experiment used two types of targets: a 100-μm-thick Cu foil and a Cu foil attached to a polystyrene (CH) hemisphere post with a quarter-inch radius (6350 μm). The surface area of the Cu foil was 1mm^2. The large CH piece allowed fast electrons to travel continuously from the Cu to the CH, preventing the electrons from recirculating to the Cu foil for further x-ray generation. Here, a low-Z backing material was chosen to minimize x-ray generation from the backing, thus making the Cu foil the dominant bremsstrahlung source. The shot-to-shot laser energy variation for the Cu target is 7.5% and 8.7% for the Cu-CH target.

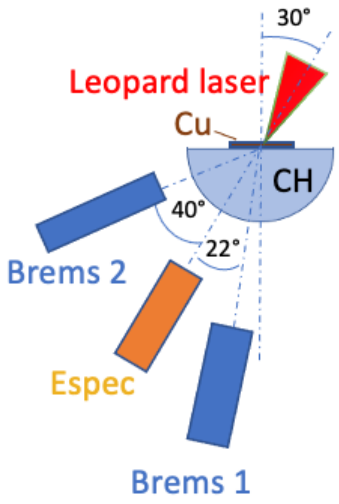

Figure 4.1 Schematic diagram of the experimental and diagnostic layout.

The magnet-based electron spectrometer introduced in Section 2.4.1 measured the escaped electrons from the target rear along the laser axis. At least two target shots were performed for each laser and target condition. Figure 4.2 shows the measured electron spectra for the Cu and Cu-CH targets. Both spectra fit well with a single exponential slope of 1.25 ± 0.15 MeV for the Cu and 1.15 ± 0.35 MeV for the Cu-CH target. A variation in measured slope temperature is attributed to shot-to-shot variations in the preplasma scale length, on-target intensity, and target alignment. In this experiment, the variation in the slope temperature is 4.0% and 4.3% for the Cu and Cu-CH targets, respectively. Some of the high energy electrons (> ~3 MeV) deviated from the single slope spectrum in our measurements, but their contribution to bremsstrahlung generation was minor, as shown in Subchapter 3.2 on electron recirculation trajectories with electrons of 5 MeV kinetic energy. The inferred slope temperatures were comparable for the two cases as expected,

given that any difference between them would arise whether the CH backing was used. The slope of the escaped electrons along the laser axis relates directly to that of the electrons generated near the laser interaction region.[85,86] The number of escaped electrons from the Cu foil was consistently higher than that from the Cu-CH target. As reported in Ref. [49,87,88], the magnitude of the rear sheath field is proportional to the square root of the electron number. As the target becomes thicker, the number of electrons escaping from the target's rear decreases due to the angular spread of the electron beam, which is consistent with the measurement.

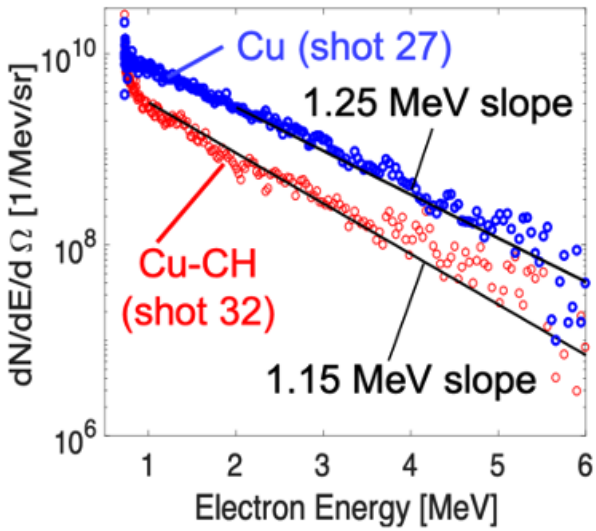

Figure 4.2 Measured electron spectra from the Leopard experiment.

Figure 4.3 shows the measured bremsstrahlung signals at +22° (Brems1) and -40° (Brems2) for both targets. The intensity of the bremsstrahlung decreased with the angular

position of the spectrometer away from the laser axis (i.e., the signal was higher at +22° than at -40°). The CH post, which prevented electron recirculation, reduced the bremsstrahlung signals by a factor of 2 in the seventh layer (~50 keV) in both detectors. These measured signals were directly compared and simultaneously fitted with LSP simulations by varying the input divergence angles and the electron beam energies, as shown in Subchapter 4.3.

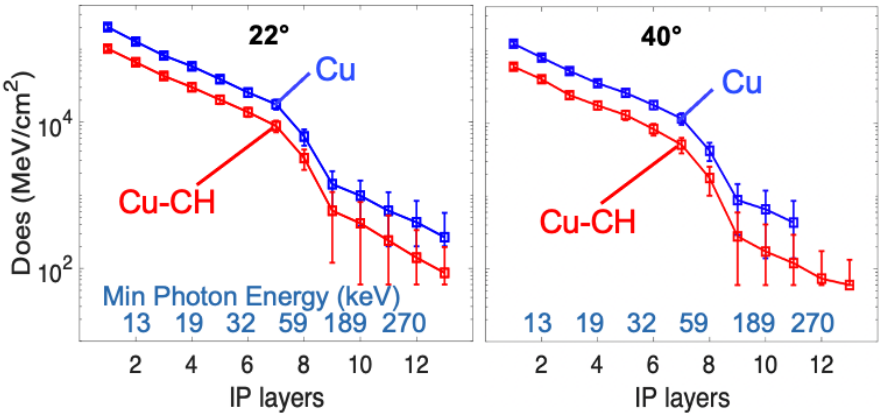

Figure 4.3 Measured Bremsstrahlung signals of the Cu and Cu-CH targets at +22° (Brems1) and -40° (Brems2)

4.2 3D LSP Modeling of Angularly Resolved Bremsstrahlung Radiation

Simulations of fast electron transport and hard x-ray generation were performed using a 3D hybrid PIC LSP code. The simulations were initiated by injecting a beam of fast electrons instead of solving a laser-target interaction. The use of 3D cartesian coordinates was essential in this work to compute the development of self-consistent fields at all target-vacuum boundaries and to model the off-axis incident angle of an injected

electron beam that mimics the laser incident angle with respect to the detector positions in the experiment. Magnetic fields generated by resistive gradients or filamentation are not included. The code takes into account the stopping power, scattering, and radiative loss for the electron transport processes.[89,90] The generation of bremsstrahlung and Kα photons in the LSP is modeled using a cross-section calculated with ITS.[91]

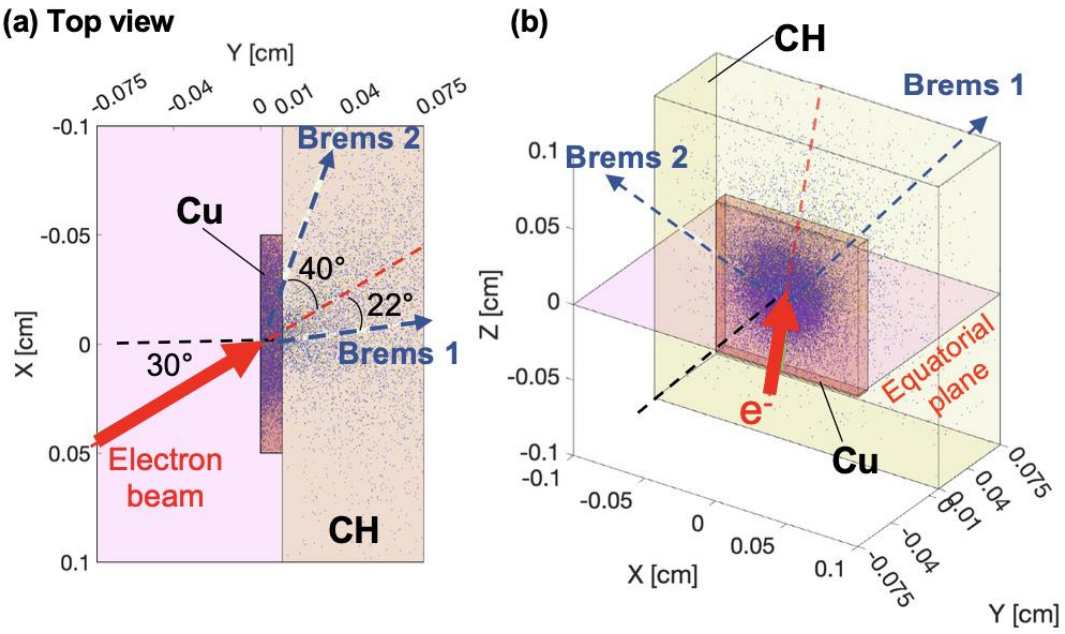

Figure 4.4 3D hybrid PIC LSP simulation setup for the Cu-CH target. (a) Top view, and (b) a 50° view from the equatorial plane. The injection axis of an electron beam and the diagnostics are both in the equatorial plane. Blue dots are fast electrons.

The simulation box size was large enough to calculate the development of electric and magnetic fields surrounding the Cu target. A 100-μm-thick Cu foil with a surface area of 1.0 mm^2 was positioned at the center of a 2.0×1.5×2.0 mm^3 simulation box with a cell

size of 10 μm, resulting in ~ 500 μm vacuum spaces all around the Cu foil. For the Cu-CH target, a 650-μm-thick plastic layer with a 2.0×2.0 mm^2 surface area was attached to the rear side of the Cu. Given that absorbing boundaries were used, the plastic reaching the boundaries was essentially an infinitely large layer. The simulation setup and the electron beam injection axis for the Cu-CH target at an incident angle of 30º in the equatorial plane are illustrated in Figures 4.4(a) and (b) in different view positions. In Fig. 4.4 (a), one can compare the electron number density (blue dots) at the Brems2 position at 70° from the target normal clockwise vs. counterclockwise to find the asymmetrical feature of the photon generation when the electron beam is injected non-normally to the target front. The duration of the electron beam was assumed to be the same as that of the laser pulse (0.35 ps FWHM), and most simulations were run for 20 ps. As discussed later, the main electron source parameters varied for fitting were the divergence angle and electron beam energy.

Photons generated in the Cu and CH layers were post-processed to compute the time- and angular-dependent photon spectra and the synthetic bremsstrahlung spectrometer doses using a spectrometer response function[53]. The time-integrated bremsstrahlung spectra and the spectrometer doses at the +22° (Brems1) and -40° (Brems2) detector positions for the Cu-CH target are presented in Figures 4.5(a) and (b). The electron parameters used for the simulation were T_h = 1.0 MeV, θ = 50°, and E_b = 1.5 J. The broadband x-ray spectrum consisted of bremsstrahlung radiation above 10 keV and the characteristic Cu K-photons near 8 keV. The calculated x-ray spectrum in Fig. 4.5(a) was converted to simulated doses for each IP layer of the spectrometer to directly compare them with the measurements in absolute units (in the following subchapter). Both the raw x-ray

spectra and the spectrometer doses showed higher signals at +22° (close to the electron injection axis) than at -40° for a T_h of ~1.0 MeV, which is the same trend as the experiment. The angular distribution of bremsstrahlung depends on the target material, the thickness of the target, and the fast electron spectrum (or laser intensity). Here, the measured anisotropy of the bremsstrahlung signals was attributed to the 100-μm-thick Cu foil because such measurements are nearly isotropic with a T_h of ~ 0.6 MeV as in a previous experiment[73]. It is reported that the isotropic hard x-ray emission originates from thin foil or wire targets (< 10 μm) due to the strong electron recirculation up to a peak laser intensity of 10^{20} W/cm^2.[92]

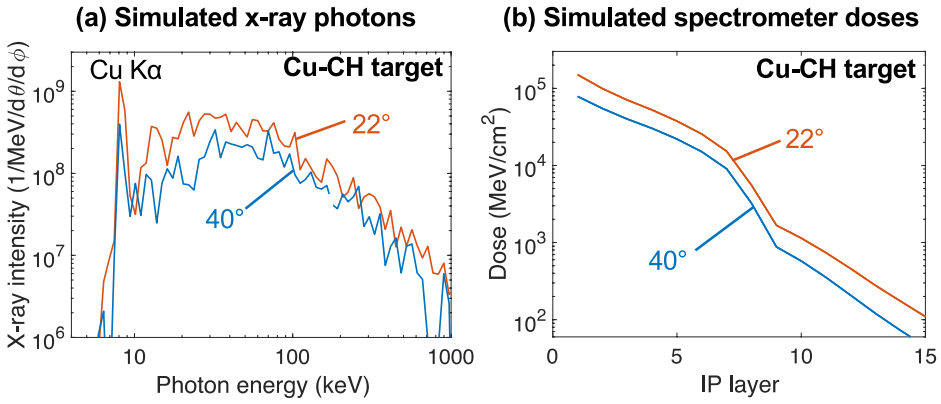

Figure 4.5 (a) Calculated bremsstrahlung spectra at the +22° and -40° positions for the Cu-CH target. (b) Synthetic spectrometer doses as a function of the IP layers after the spectra in (a) are processed using a detector response function.

To directly compare the simulation and measurement at the same unit, both measurements and simulation results are converted to values in an absolute unit of MeV/cm^2. Figure 4.6 shows the detailed procedure of the unit conversion from experimental measurement and simulation. From LSP simulations, results of time-integrated bremsstrahlung signals have a unit of the photon number per polar angle (*theta*, θ) and azimuthal angle (*phi*, ϕ). This unit can be converted to a unit of MeV/cm^2 using the spectrometer response matrix described in Chapter 3. On the other hand, the experimentally measured bremsstrahlung signals have a unit of PSL/Pixel^2. Considering a conversion of the PSL value to dose in energy and IP resolution, the experimental values recorded with the spectrometer can be converted to MeV/cm^2. After these unit conversions for experimental and numerical results, a direct comparison between the measurements and calculations is performed, as shown in the following subchapter. The conversion efficiency from laser to fast electrons cannot be obtained by comparing bremsstrahlung calculations from 2D simulations.

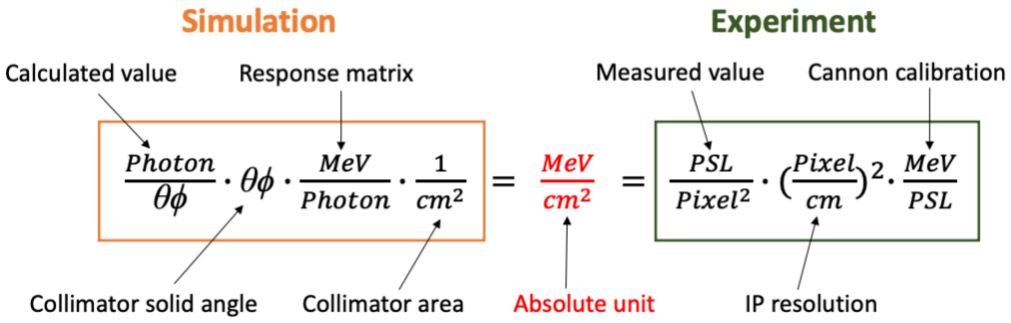

Figure 4.6 The procedures to convert calculated and measured signals to an absolute unit.

4.3 Results and Discussions

4.3.1 Fitting to the Bremsstrahlung Measurements for the Cu-CH Target

Comparisons of the simulations to the measurements were first performed for the Cu-CH target in which the CH backing essentially eliminates electron recirculation. The measured bremsstrahlung doses were fitted with a series of LSP simulations by changing the electron beam energy, E_b, and the divergence angles, θ, while the fast electron slope temperature was fixed in the range of the electron spectrometer measured value (1.15 ± 0.35 MeV). The ranges of E_b and θ were varied from 0.5 to 2.0 J and 10° to 90°, respectively. For each spectrometer, the fitted residuals between the measured and simulated doses were calculated using the chi-squared method, in which the chi-squared value was examined by calculating $\chi^2 = \sum_{i=1}^{n} \frac{(y_{exp}-y_{sim})_i^2}{\sigma_i^2}$, where y_{exp} and y_{sim} were the measured and simulated bremsstrahlung doses at the i-th layer of IP, respectively, σ_i was the standard error of each measurement, and n was the total number of the IP layers. For each electron beam energy and divergence angle, the chi-squared values were separately calculated for two bremsstrahlung spectrometers at +22° and -40°. Figures 4.7(a) ~ 4.7(c) show the chi-squared map in each spectrometer direction and a combined chi-squared map with T_h=0.8 MeV. The results show that a minimum chi-squared value for Brems1 appears near E_b = 1.0 J and θ = 70°, but separated islands are found for Brems2. By combining the two chi-square maps, a range of the divergence angle and beam energy with which the simulations are closest to the measurements can be found. The contour map with additional fitting results was smoothed to infer a range of the electron parameters with errors.

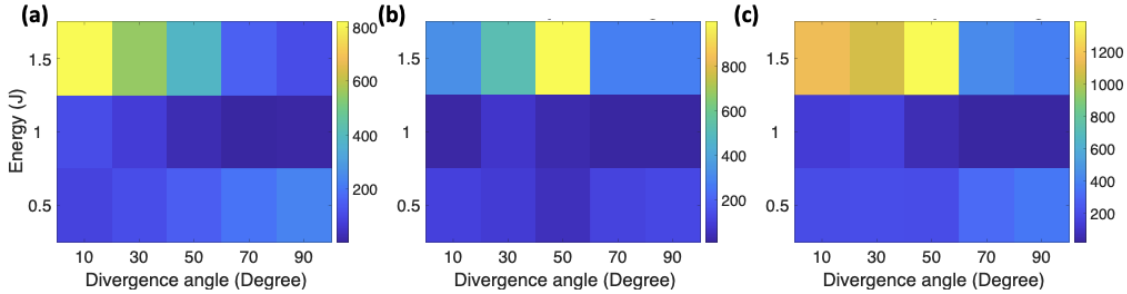

Figure 4.7 (a) Raw chi-squared value map of (a) at +22° (Brems1), (b) at -40° (Brems2), and (c) Brems1+Brems2.

Figure 4.8 shows contour plots of the smoothed chi-squared values for the Cu-CH target with the slope temperature of 1.15 MeV and 0.80 MeV. The color bar represents the normalized chi-squared value of the corresponding color. In Fig. 4.8(a), the contour map for a T_h of 1.15 MeV shows a well-defined region in the range of 52° ± 8° and 1.6 ± 0.2 J, estimated from an area of two times the minimum chi-squared value. In Figs. 4.8(b) and 4.8(c), the simulated doses using the best-fit parameter are compared with the experimental doses. The result shows a good agreement for Brems1 but a slight deviation for Brems2. On investigating the dependence of the slope temperature on the fitting, a better agreement between the experiment and the simulation was found with a lower T_h than that from the measured electron spectrum. Figures 4.8(d) ~ 4.8(f) show a contour map of the chi-squared values for a T_h of 0.8 MeV and comparisons of the measured and simulated doses using θ = 70° and E_b = 1.3 J. The range of θ and E_b inferred from the contour map for a T_h of 0.8 MeV is estimated to be 75° ± 15° and 1.3 ± 0.2 J. As shown in Fig. 4.8(f), the agreement

is better with a T_h of 0.8 MeV, indicating that the slope of the electron energy distribution in the laser-interaction region may be lower than that of the escaped electron spectrum. Using the slope temperature of a measured electron spectrum can be a good starting point for fitting. However, an additional parameter study, the electron energy spectrum in this case, is necessary to find a unique set of laser-driven fast electron parameters. In this work, all three electron characteristics have been determined by comparing the fitting results for both the Cu-CH and Cu targets, as shown in the following subchapter.

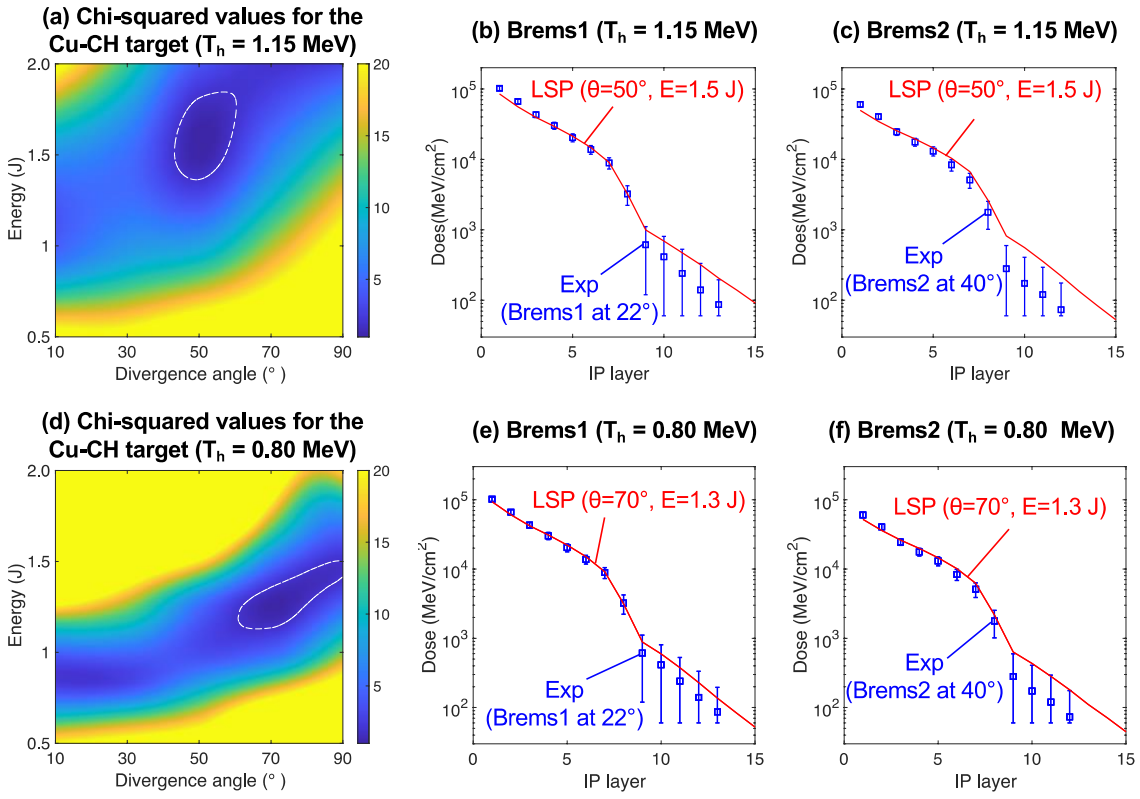

Figure 4.8 (a) Contour map of chi-squared values of the fitting result for the Cu-CH target. The contour is a combined result for the fits to the data for both spectrometers. The white dashed lines indicate twice the minimum value in the range of θ=52° ± 8° and E_b=1.6 ± 0.2

J. The color bar shows the chi-squared values. The measurements are compared with a simulation using the best-fit parameter (θ=50°, E_b=1.5 J, T_h=1.15 MeV) for (b) Brems1 and (c) Brems2. (d) Contour map of chi-squared values for T_h=0.80 MeV. The dashed line indicates the range of θ=75° ± 15° and E_b=1.3 ± 0.2 J. (e, f) Comparisons of the experiment with a simulation using θ=70° and E_b=1.3 J at the +22° and -40° positions.

4.3.2 Fitting to the Bremsstrahlung Measurements for the Cu Target

Fitting of the parameters to the measured bremsstrahlung, similar to that for the Cu-CH target in the previous section, was performed for the strongly refluxing Cu target. An experimental slope temperature of 1.25 MeV, as shown in Fig. 4.2, was chosen for the fitting. Figure 4.9(a) shows a contour plot for the chi-squared values for the fitting results for the Cu target. A narrow region of low chi-squared values was found in the electron beam energy across a range of divergence angles, from 10° to 90°. Figures 4.9(b) and 4.9(c) show a comparison of the experimental results for three simulated spectrometer doses of θ=10°, 50°, and 90°, respectively. The variation in the input divergence angle did not change the simulated doses, particularly for Brems2, as shown in Fig. 4.9(c). The simulation result indicates that the initial divergence angle of an injected electron beam could not be retrieved from modeling the angularly resolved sub-MeV bremsstrahlung radiation from a strongly refluxing target. However, fast electron characteristics can be deduced by combining the fitting results for both the Cu-CH and Cu targets.

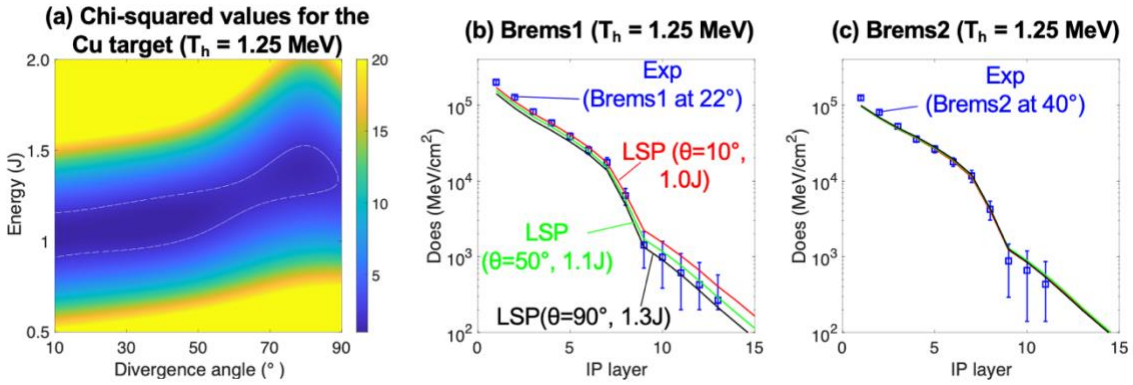

Figure 4.9 (a) Chi-squared map of the fitting result using a T_h of 1.25 MeV for the Cu target. Comparisons of the experimental results with the simulated doses for different divergence angles and beam energies for (b) Brems1 and (c) Brems2.

4.3.3 Determination of Fast Electron Characteristics

The two types of targets used (bare Cu and Cu-CH) were irradiated by the same laser condition. It is reasonable to presume that fast electrons with similar characteristics are generated on the surface of the Cu foil in both targets. This assumption allows us to find the overlapping parameter space in Figures 4.8(a), 4.8(d), and 4.9(a). The divergence angle and the beam energy estimated for the Cu-CH target with a T_h of 0.80 MeV (75° ± 15° and 1.3 ± 0.2 J) are consistent with the results for the Cu, whereas no common parameter area was found in the case of T_h of 1.15 MeV or 1.25 MeV. Comparisons of the measurements with simulations for a T_h of 0.80 MeV are presented in Figures 4.10(a) and (b). The simulations reproduce well the differences in the bremsstrahlung doses between the Cu and the Cu-CH at both detector positions. The results demonstrate that measurements of the angularly resolved bremsstrahlung signals and escaped electrons from

a metallic x-ray source target with and without a large low-Z layer constitute a benchmark data set that can be used to test electron recirculation physics in numerical modeling.

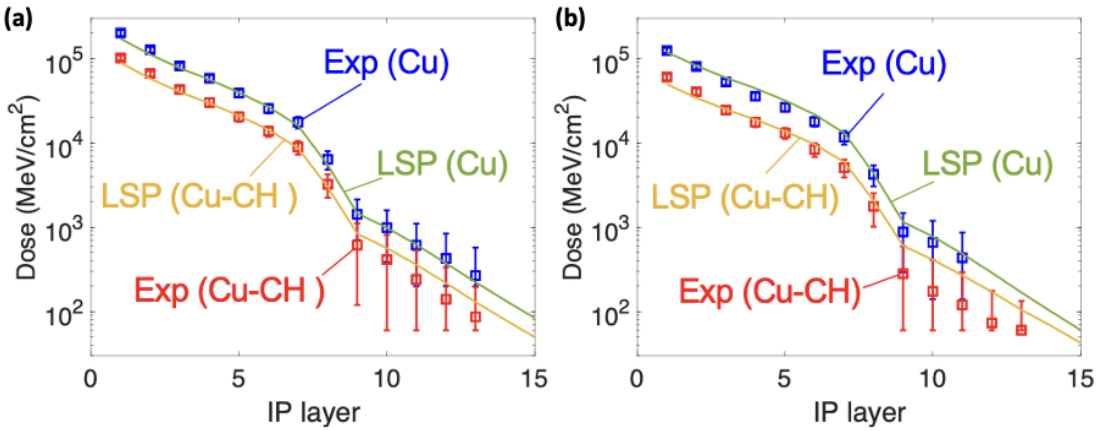

Figure 4.10 Comparisons of the experimental results with the simulated doses with θ=70° E_b=1.3 J, and T_h=0.80 MeV for (a) Brems1 and (b) Brems2.

The divergence angle inferred in this study (θ=75° ± 15°) is significantly larger than that found in previous work using 2-D LSP simulations (θ=15° ± 8°)[75]. The LSP code in a 2-D Cartesian geometry can appropriately incorporate the electron injection axis and the electron recirculation in simulations. However, the transport of fast electrons is solved only in a two-dimensional plane, and the absolute photon yields cannot be calculated due to an open system being used. Thus, simulated doses from the 2-D simulations were compared with those from the experiment using arbitrary units. Different divergence angles inferred from the present 3D and previous 2-D LSP simulations suggested that modeling of the electron recirculation must be performed in a 3D space. The results that produce a larger

divergence angle using a 3D rather than a 2-D simulation are consistent with the results of implicit 2-D and 3D PIC simulations.[93]

The conversion efficiency from the laser to fast electrons in a single-slope temperature spectrum was estimated to be 8~10% for this particular shot, with a laser energy of 14.8 J. This value is a lower bound because the electron energy distribution is assumed to be the single slope of the electron spectrum. It is well known that the energy distribution of fast electrons generated in the laser interaction region is described by a continuous spectrum of electrons that can be represented as a sum of multiple exponential slopes. Low-energy electrons (< tens of keV) contribute less to producing the bremsstrahlung radiation used for this analysis, so the bremsstrahlung measurements would be ineffective in realizing a low-energy component. Given that these electrons are trapped by strong magnetic fields in a preplasma or collisionally stopped near the target surface, diagnosing the low-energy component of the spectrum requires alternative measurement techniques. Including the other electron energy components in the single-slope spectrum would increase the total electron beam energy and conversion efficiency.

4.4 Summary

This chapter presents the characterization of sub-ps laser-produced fast electrons by modeling angularly resolved bremsstrahlung measurements for the refluxing and non-refluxing targets with the 3D hybrid PIC LSP code. The bremsstrahlung and escaped electron measurements were made for the strongly refluxing 100-μm-thick Cu foil and a non-refluxing Cu foil with a large CH layer. The divergence angle and conversion

efficiency were determined from the simultaneous fitting of the two bremsstrahlung signals with simulations. At the same time, a slope temperature of the electron energy spectrum was estimated from the electron measurement. It was found that all three electron parameters could not be determined uniquely from either fitting to the Cu-CH or the Cu data. However, assuming the same electron source was generated in both targets, agreements between the simulation and experiment were found for both datasets using the divergence angle and beam energy (conversion efficiency) of 70° and 1.3 J (8.9%), respectively, for a slope temperature of 0.8 MeV. The results demonstrate that angularly resolved bremsstrahlung measurements from a metal foil with and without a large low-Z layer to control electron recirculation can provide benchmarking data for a 3D hybrid PIC code.

5. Numerical Studies of a Bremsstrahlung Source for Hard X-Ray Radiography

The benchmarked 3D hybrid PIC LSP code, as shown in Chapter 4, allows numerical studies of temporal- and spectral-resolved x-ray generation during the transport of fast electrons in the target. This is particularly useful in a situation where spatial, temporal, and spectral resolutions of diagnostics are limited. In this chapter, two numerical works were conducted using the benchmarked LSP code. Subchapter 5.1 presents time-resolved bremsstrahlung x-ray generation between the refluxing and non-refluxing targets. Subchapter 5.2 describes the effect of CH backing size on mitigating electron recirculation in the Cu target.

5.1 Calculations of Time-dependent Bremsstrahlung Radiation Between Refluxing and Non-refluxing Targets

Currently, no ultrafast time-resolved broadband hard x-ray diagnostic is available. Numerical studies on the time-dependent bremsstrahlung generation are particularly insightful for understanding the physics of electron recirculation. Two simulations were performed for refluxing and non-refluxing targets with and without a plastic layer using a slope temperature of 0.8 MeV, a divergence angle of 50°, and a beam energy of 1.3 J, respectively. Figures 5.1(a) and 5.1(b) show the temporal evolutions of the bremsstrahlung spectra between 10 and 2000 keV at the +22° and -40° detector positions. The spectral intensities are comparable up to ~2 ps. After 2 ps, the x-ray spectral intensity profile for

the Cu become much higher than that for the Cu-CH target by a factor of ~2.2 (~3.3) at +22° (-40°) around 100 keV at 20 ps [differences between the red (2 ps) and blue (20 ps) curves in Fig. 5.1(a) and (b)]. The phenomenon of an enhancement in the x-ray yields due to electron recirculation is well known. Here, the simulation shows, for the first time, that the bremsstrahlung spectrum peaking at ~ 70 keV continues to increase with time.

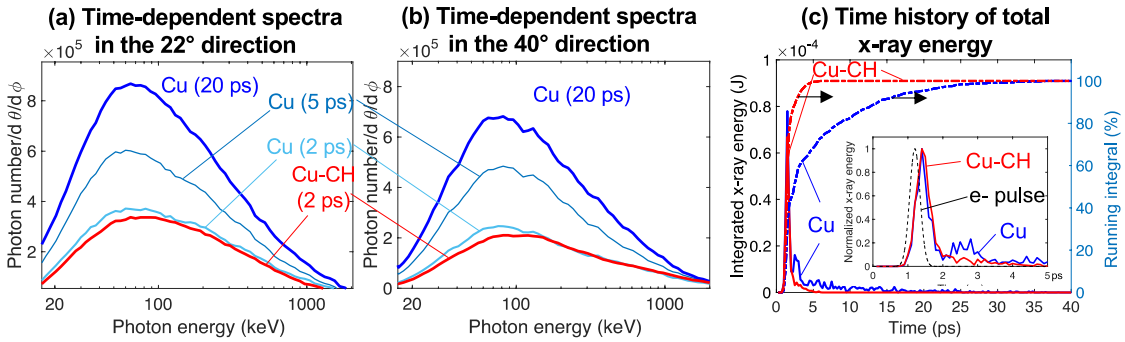

Figure 5.1 (a) Temporal evolution of calculated bremsstrahlung spectra between 10 and 2000 keV at the +22° position and (b) at -40° position. (c) A time history of spectrally integrated x-ray energy between 70 and 200 keV along the +22° direction for the Cu and Cu-CH targets. Dashed lines represent running integrals of the x-ray energies as a percentage. The inset in (c) shows the normalized time history for up to 5ps with the 0.35 ps electron pulse peaked at 1.2 ps. The FWHM of the x-ray pulses is 0.39 ps and 0.48 ps for the Cu and Cu-CH targets, respectively.

To examine the duration of the x-ray emission, the bremsstrahlung spectrum was integrated with respect to the photon energy between 70 keV and 200 keV, whose spectral range is an effective backlighter spectrum for broadband x-ray radiography (Compton

radiography) of an ICF implosion core.[94,95] Figure 5.1(c) shows the time histories of the integrated x-ray energy for the Cu and Cu-CH targets in the +22° detector direction. The inset in the figure shows the time between 0 and 5 ps, along with the electron pulse history. The rising edge of the x-ray generation and the time of the x-ray peak are almost identical for both targets. These traces start to diverge from one another after the x-ray production reaches a peak around 1.5 ps, which is slightly later than the peak of the electron pulse at 1.2 ps. [see black dashed line in the inset of Fig. 5.1(c)]. The x-ray intensity of the Cu-CH target rapidly decays as the electron beam exits from the Cu foil at around 2.5 ps and becomes zero at ~5 ps. In contrast, electron recirculation in the Cu foil produces weak x-ray emission for ~ 25 ps. In Fig. 5.1(c), running integrals of the x-ray energy history are calculated and plotted as dashed lines. These plots reveal that 95% of the x-ray energy between 70 and 200 keV is produced within 3 ps for the Cu-CH target, while reaching 95% for the Cu target takes ~25 ps, although 50% of the x-ray energy is produced in ~ 3 ps. It is important to note that the duration of the x-ray emission presented here is an upper limit because (1) the simulations exclude a proton layer on the rear side of the target that weakens the magnitude of the sheath potentials when they are accelerated via TNSA, reducing the number of recirculated electrons, and (2) the thermal expansion of the target due to heating is neglected. Nonetheless, this result indicates that care must be taken when a rapidly evolving object, such as a laser-driven implosion core, is radiographed with a laser-driven x-ray source using an isolated solid target. Such a long-lasting x-ray emission due to electron recirculation has been measured in a radiography experiment at NIF. An x-ray streak measurement has shown that a spectrally integrated x-ray emission persists over

~300 ps when a 30 ps NIF ARC beam irradiates an Au wire target.[95] 3D hybrid PIC modeling of time-dependent sub-ps laser-produced bremsstrahlung could be extended to simulate the electron transport and bremsstrahlung generated by multi-ps short-pulse lasers.

5.2. Mitigation of Electron Recirculation Using Various Volumes of Plastic Backing

The second numerical study is on the suppression of electron recirculation and hard x-ray generation with various volumes of plastic backing. In high-intensity laser experiments, a large volume of low-Z material attached to a primary target is often used to reduce electron recirculation. However, the minimum dimensions of such a backing are not understood well. Finding the minimum volume of plastic necessary to eliminate the effects of electron recirculation by using LSP in a 3D configuration is conducive to obtaining simulation box sizes and designing refluxing-controlled targets for experiments. Here, a series of 3D LSP simulations are performed by varying the thickness and surface area of a CH backing from 100 μm to 650 μm and from 1.0 mm^2 to 2.0 mm^2, respectively. The electron parameters used in the simulations are T_h = 0.8 MeV, θ = 50°, and E_b = 1.3 J. Figure 5.2 shows calculated spectra of the space-integrated hard x-ray photons generated in a 100-μm-thick Cu foil with different volumes of CH backing. X-ray attenuation by the target itself was not taken into account and calculated for the spectra. Adding a CH backing to the Cu reduces the photon spectrum uniformly over a broad photon energy range up to ~ 1.0 MeV. Attaching a 500-μm-thick CH with a 1.0 mm^2 surface area to the Cu decreases

the spectral intensity by a factor of ~2. However, this reduction is insufficient to eliminate electrons recirculating back to the Cu completely. A photon spectrum for an infinitely large CH slab is reproduced when a 500-μm-thick CH slab is used with an infinite surface area (2.0 mm^2), or an infinitely long thick slab is used with a 1.0 mm^2 surface area (not shown in Fig.5.2). This indicates that the effects of electron recirculation can be suppressed with at least a 500 μm thick plastic layer and a large surface area (> 2.0 mm^2) for a T_h of 0.8 MeV. It is noted that the minimum volume of plastic required for diminishing the effects of electron recirculation would change with a peak laser intensity generating an electron energy distribution.

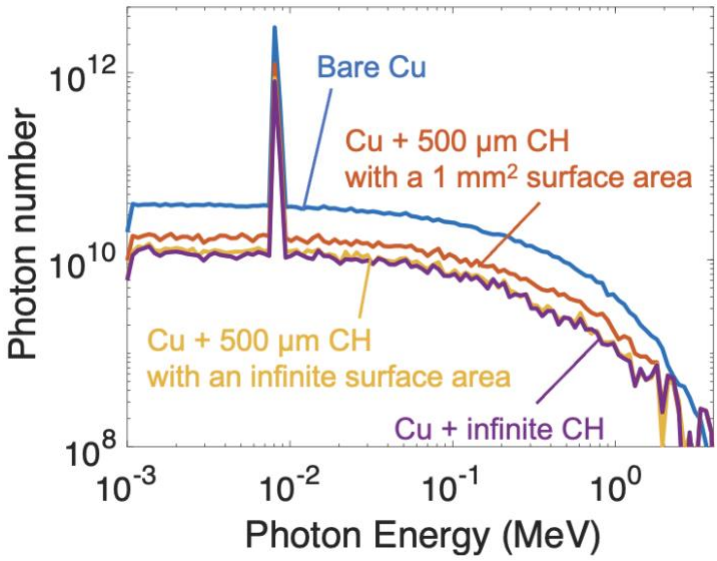

Figure 5.2 Simulated hard x-ray spectra from a 100 μm thick Cu foil with various CH backing volumes (no backing, 500 μm thick×1.0 mm^2, 500 μm×2.0 mm^2, and 650 μm×2.0 mm^2 backings).

6. Numerical Study of Various Thicknesses Ag Foil Produced Broadband X-ray Source for Radiography of a Magnetically Compressed Al Wire

A Mega-Ampere (MA) current from a pulsed power generator has been used to create high-energy-density plasmas by compressing a gaseous or solid sample with a J×B force. At UNR's Zebra pulsed power laboratory (ZPPL), we have investigated the creation of warm dense matter by cylindrically compressing a millimeter diameter Al rod and the development of a short-pulse laser-produced hard x-ray for x-ray radiography of the compressed Al. The author participated in the first laser-pulsed power x-ray radiography experiment in 2021 and performed 3D hybrid PIC simulations to optimize x-ray source targets. This chapter presents a summary of the experiment with major issues that hindered obtaining x-ray radiographic images of a compressed rod and numerical modeling to improve broadband x-ray intensities for various silver foil targets for coupled experiments in the future.

6.1 The Laser-pulsed Power-coupled X-ray radiography Experiment at ZPPL

ZPPL houses a 1 MA pulsed power generator, Zebra, and a 50 TW short-pulse laser, Leopard. As described in Chapter 1.1, the Leopard laser pulse can be delivered to either a Phoenix vacuum chamber for laser-only shots or the Zebra vacuum chamber for

coupled shots. On Zebra, surface plasma formation on a magnetically driven thick Al rod has been studied using an optical shadowgraphy[96]. However, plasma conditions of high-density regions of the rod above the critical density have yet to be experimentally determined. The project aims to diagnose a magnetically compressed high-density Al rod in x-ray radiography using a Leopard laser-produced hard x-ray source. Probing a 1.0 mm diameter solid Al requires x-ray photons greater than 10 keV. The first objective is to successfully record a radiographic image of a compressed Al wire with a broadband x-ray source in a coupled shot. For accurate density estimation, this experimental platform could be extended to performing monochromatic x-ray imaging with a laser-produced Kα x-ray source.

The first coupled x-ray radiography experiment was carried out in April 2022. Figure 6.1 shows a simplified schematic of the. A 1.0 mm diameter aluminum rod (1100 Al alloy) held by an Al anode-cathode current return cage was installed vertically in the center of the Zebra chamber as the load. A 100 ns rise-time, 0.9 MA Zebra current run through and cylindrically compresses the rod. The Leopard laser irradiated a metal x-ray source target 2.5 cm away from the Al rod. The laser was incident at ~11° from the target normal, with a spot size of 25 μm and a 0.35 ps pulse duration. Broadband x-rays generated at the target propagated through the Al rod to form an x-ray radiographic image of the rod on an IP detector. The edge-on direction of the foil target was chosen as the radiation axis for the sake of a better resolution on the image . Low energy x-rays below 10 keV were attenuated by a 5~10 mm thick nylon piece in front of the IP.

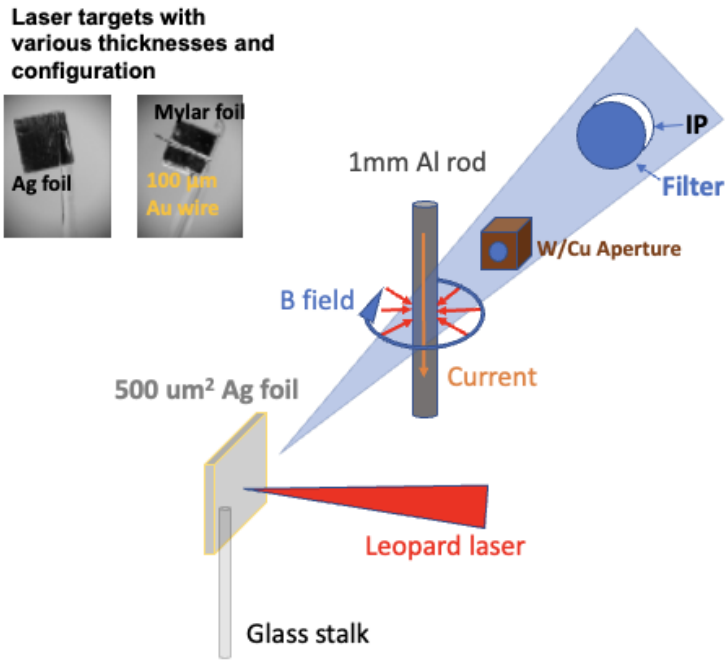

Figure 6.1 A schematic of the ZPPL experiment.

Radiographic images of a cold Al rod were obtained in several laser-only shots. Figure 6.2 shows x-ray radiography signals and images of a 1.0 mm diameter Al rod in Leopard laser-only shots. The image of an 1150 µm diameter cold Al wire with a 25 µm CH coating on the top of Fig. 6.2 was obtained in 2018 with x-rays generated by irradiating a 10 µm thick Ag foil[73], and the other radiographic image of a 1.0 mm Al rod was obtained in 2022. The x-ray signal intensity outside the Al rod was ~0.9 PSL for the 2018 campaign after a 10 mm CH filter to cut off photons below 10 keV, and the signal is ~0.07 PSL for the 2022 campaign after a 5mm Nylon filter to cut off photons below 7 keV. Several different types of targets were tested, including various thicknesses of Au and Ag foils and

an Ag/Au wire attached to a mylar. However, unattenuated x-ray signals recorded on the IP with those x-ray source targets were on the order of ~0.1 PSL or lower. The weak x-ray intensity observed in 2022 could be attributed to (1) mispositioning of the x-ray source target due to a change in the laser irradiation configuration from the 2018 campaign, (2) degradation of the laser system causing a lower laser energy delivered to the target than the past experiment, and/or (3) the target fabrication (e.g., curled foil surface). Once Zebra was fired, the IP for x-ray radiography was saturated (> 15 PSL with a 25 μm scanning resolution) by strong radiation produced inside the chamber. With additional lead shielding, IP signals were reduced below the saturation. However, it was still larger than 0.5, several times higher than the signal from the laser-generated x-ray, masking the image of the Al rod on IP.

This experiment revealed two major issues preventing us from obtaining x-ray radiographic images of a driven Al rod: (1) strong background radiation in Zebra shots and (2) weak laser-produced x-rays compared to the past experiment. In a MA pulsed power chamber, x-ray radiations inside and outside the chamber can be generated from electrical discharges between insulator gaps, the interaction of accelerated electrons with a return current cage, and the load itself. Moreover, these background radiations are likely produced after the current peak. Since the IP detector is static and the temporal resolution is set by the duration of x-ray emission produced by the laser pulse (0.35 ps), it is required to develop a radiation-shielded enclosure with a collimator. Our group member, Steven Buitron, used a Monte Carlo code to design and simulate a detector (IP) housing made with a tungsten-copper alloy for his senior thesis[97] to solve the first issue. To overcome the

second issue, we performed 3D LSP simulations to investigate angular-dependent x-ray intensities for various thicknesses of silver foil targets, as shown in the next subchapter.

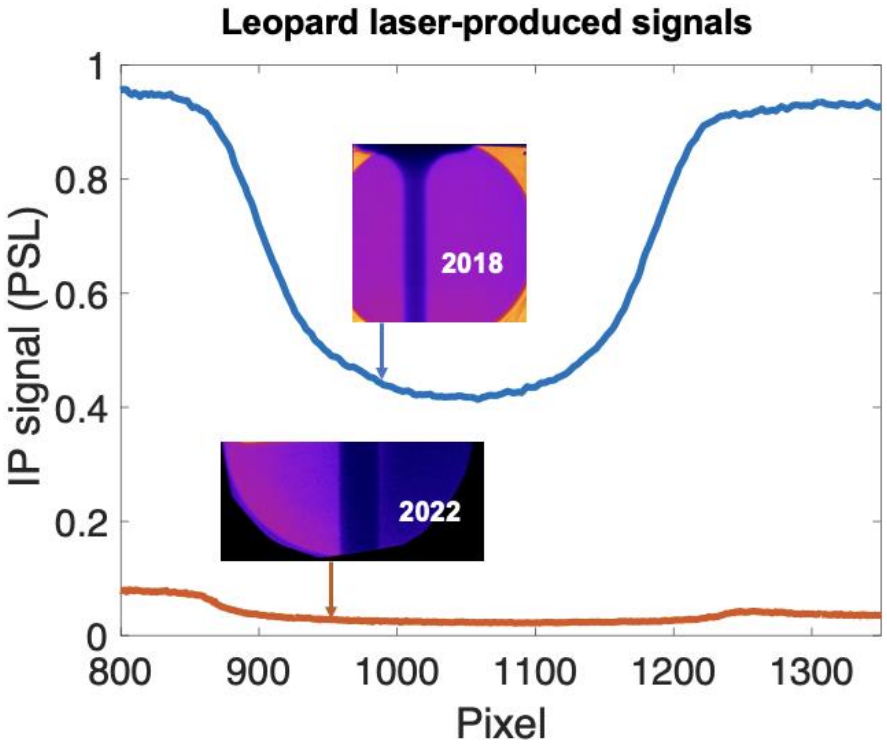

Figure 6.2 Measured laser-produced x-ray radiographic signals and images of Al rods obtained from experiments in 2018 and 2022.

6.2 Investigation of Angular-dependent X-ray Intensities for Various Thicknesses of Silver Foil Targets Using 3D LSP Simulations

Broadband x-rays produced in the short-pulse laser-target interaction have angular dependence. In the laser irradiating a thin foil with a surface area smaller than 1.0 mm^2, fast electrons strongly recirculate, inducing x-rays from the entire target. For improving spatial resolution by minimizing the source broadening for x-ray radiography, it is proposed to use x-rays emitting along the foil surface[98]. The experiment presented in Chapter 6.1 used this edge-on geometry for recording x-ray images, along which the x-ray intensity is the lowest in an angular distribution due to attenuation by the target. This chapter, therefore, presents a numerical investigation of broadband x-ray intensities as a function of angular distributions and target thicknesses. Simulation results evaluate increases in an x-ray source intensity at the expense of spatial resolution up to the target size.

A series of 3D LSP simulations were performed for various thicknesses of silver foil targets. The input electron parameters were fixed to the injected fast electron beam energy of 1.0 J, the divergence angle of 70°, and the energy slope temperature of 0.3 MeV. The first two parameters are chosen based on the result of the Leopard experiments (Chapter 4), and the slope temperature is a value measured in the coupled experiment in 2022. The simulation box sizes are chosen to have large vacuum spaces for accurately modeling electron recirculation. The foil thickness varies from 10 μm to 300 μm, and the surface area is fixed to 500×500 μm^2. The electron injection angle is 11° from the target

normal, the same as in the experiment. Simulated x-ray signals are averaged over ±20° below and above the equatorial plane to calculate angularly resolved x-ray spectra.

Figure 6.3 shows a polar plot of the calculated photon number distribution for various thicknesses from 10 to 300 μm. The angular photon distribution is calculated by integrating the energy spectrum from 10 to 100 keV and averaging the signals over 10°. The electron beam is injected in the direction of 270° in the polar plot. The figure shows relatively weak x-ray intensities in the edge-on direction at 0° and 180°. The x-ray intensities in the edge-on direction for the 10-300 μm thick target are less than 30% of the intensity in the target's normal direction. By changing a detector position from the side to the front, the integrated x-ray intensity could be tripled. Fig. 6.3 also shows that a thicker Ag target attenuates the x-ray significantly in the forward directions due to the longer attenuation length than those from thinner targets. In particular, the photon number (10-100 keV) in the target normal forward direction generated by a 10 μm thick target is more than 6 times that of a 300 μm thick target, indicating that x-ray source generated by a 10 μm thick Ag target in the forward direction is preferable for x-ray radiography. Besides the thickness, attention also needs to be paid to the target surface area. Simulations with various thicknesses of Ag foil show that the whole target emits x-rays, so a smaller surface area could help to increase the image's resolution when the target forward normal is used as the radiographic direction.

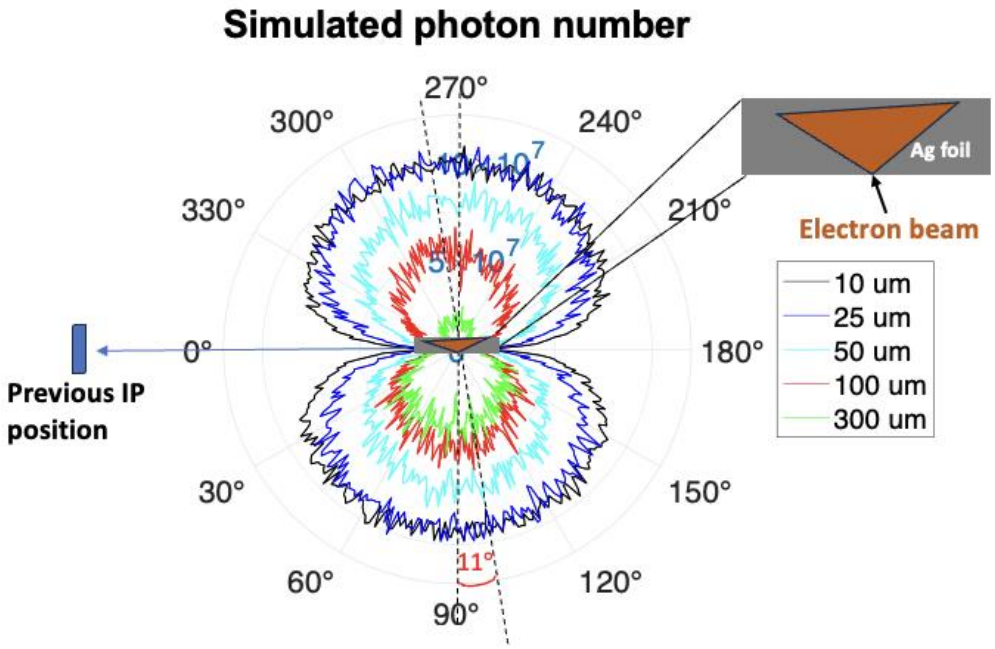

Figure 6.3 A polar plot of simulated photon number of different thicknesses on the equatorial plane (averaged over ±20°).

Figure 6.4 (a) shows calculated broadband x-ray energy spectra for various target thicknesses in the target normal direction and the PHITS calculated IP sensitivity curve. The x-ray spectrum above 100 keV is unchanged as the foil thickness increases. The major difference in the x-ray spectrum is observed in the range of 10 and 100 keV. The photon number increases as the target thickness decreases until it reaches a maximum when the thickness is 10 μm and 25 μm. Between 10 and 25 μm thick foils, the intensity change can be explained by decreasing the slope of the bremsstrahlung radiation as the target thickness decreases. This can be seen below and above the characteristic x-ray lines (~22 keV Kα

and 28 keV Kβ). As shown in Fig. 6.4 (a), the x-ray spectrum for the 10 μm thickness above the line emission is slightly lower than that for 25 μm, indicating that the generation of bremsstrahlung radiation from the 10 μm target decreases (i.e., less electron propagation distance). In contrast, the spectral intensity below the line emission for 10 μm is consistently higher than 25 μm since the lower energy photons are attenuated less in the case of 10 μm thickness. The blue curve in Fig 6.4 (b) shows the calculated unattenuated Kα photon numbers of different target thicknesses, and the magenta curve shows the calculated relative IP signals (including attenuation) using the PHITS calculated IP sensitivity curve in Fig 6.4 (a). The thickness dependence of the photon generation can be explained by, in general, that two factors compete during the generation of the bremsstrahlung radiation. One is the propagation distance of the fast electrons in the target. If electrons travel only one pass in the target (high energy electrons), a thicker target should generate more bremsstrahlung photons. However, the electron recirculation due to the sheath field around the target makes low energy electrons move inside the thinner targets several times and generates a similar number of photons as the thicker ones in the range of 10-300 μm. As shown by the blue curve in Fig 6.4 (b), in which one can find that the unattenuated Kα photon numbers are similar [less than 10% difference from the highest one (25 μm) to other cases]. The second factor is the attenuation length of the target itself. A large portion of photons generated by a thick target is attenuated during the transport in the target. For example, 300 μm Ag attenuates almost all photons below 30 keV, and the highest transmission is 6.4% for the silver K-edge energy (25.5 keV). Consequently, as the magenta curve in Fig. 6.4(b) shows, the 10 μm target does not generate the most photon

number among all thicknesses, but significantly less attenuation by the target itself ensures the resultant IP detected signal is highest in the photon energy range of 10-100 keV. Here the range 10-100 keV is chosen because this is not only the IP's most sensitive photon energy range but also the most effective photon energy range to infer the density profile of a 1 mm diameter Al rod. Due to the limitation of the hybrid PIC code (hard to simulate the electron transport and photon generation with a thinner than 10 μm target inside a larger than mm size simulation box), thinner targets are not simulated.

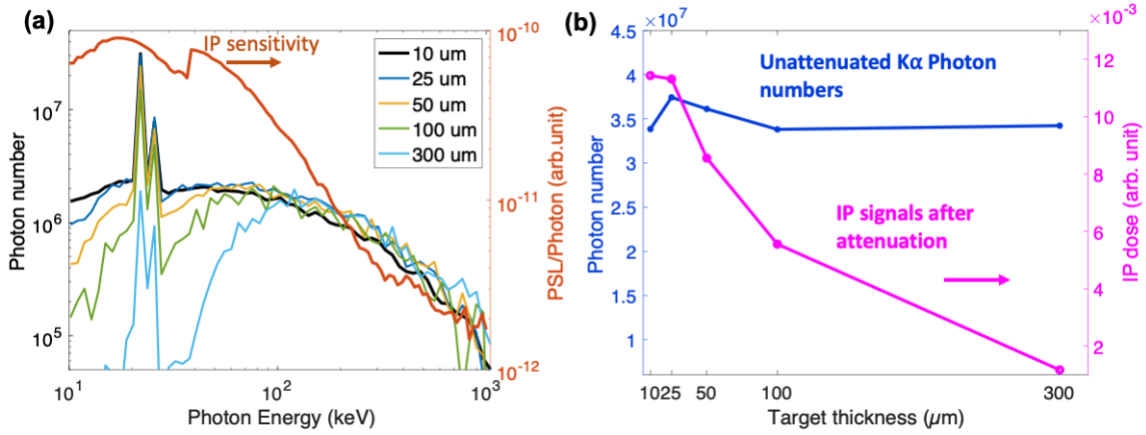

Figure 6.4 (a) The photon spectrum comparison of various thicknesses in the target normal direction and the PHTIS calculated Fuji BAS-MS IP sensitivity curve. (b) The unattenuated Kα photon numbers (blues curve) and the calculated IP signals (magenta curve) of each target thickness.

In conclusion, x-ray radiographic images were obtained in the Leopard laser-only shots performed in UNR's ZPPL, and a series of 3D hybrid PIC simulations were used to investigate the x-ray generation's laser target thickness dependence. The thickness of 10

μm proved to be the best option among various thicknesses between 10 and 300 μm by comparing the simulated x-ray photon number in the energy range of 10-1000 keV and the calculated relative IP signal. Regarding taking advantage of a higher photon intensity, the forward target normal should be chosen as the direction to place the radiographic IP.

7. Summary and Future Work

This thesis is devoted to experimental and numerical investigations on characterizing high-intensity short-pulse laser-driven fast electrons by modeling angularly resolved bremsstrahlung radiation using the 3D hybrid PIC code LSP. Understanding the fast electron parameters of the electron energy spectrum, divergence angle, and laser-to-electron conversion efficiency is crucial for advancing the knowledge of high-energy-density science and applications, including fast ignition inertial confinement fusion and secondary source generation with relativistic intensity terawatt- and petawatt-class lasers.

For fast electron characterization, a Leopard laser experiment was conducted to measure particle and radiation data for a 100 μm Cu foil or the foil attached to a CH backing irradiated at an intensity of ~2×10^{19} W/cm^2. Laser-driven MeV fast electrons traverse and recirculate within the target, generating bremsstrahlung radiation. Spectrally resolved bremsstrahlung radiations and escaped electrons were measured at two angular positions and along the downstream of the laser beam, respectively. Collecting the data from the two target types allowed us to study the effect of electron recirculation (refluxing) on the bremsstrahlung generation, primarily in the Cu foil. For simulating angular-dependent bremsstrahlung radiations, the LSP code in a 3D cartesian coordinate was used to fully model fast electron recirculation behavior and incorporate the incident electron beam angle. The slope of an electron energy distribution was initially chosen from the measured spectrum. Then, the divergence angle and injected electron beam energy were determined from an extensive parameter study by comparing the measured and simulated bremsstrahlung doses. By combining the fitting results for the Cu and Cu-CH targets, a set

of all three electron parameters (T_h=0.8 MeV, θ=70°, and E_b =1.3 J) was found to reproduce the experimental measurement. This work demonstrated the fast electron characterization that uniquely determines all three parameters for the first time.

With the benchmarked code, the effects of fast electron recirculation on the generation of bremsstrahlung radiation were numerically investigated. First, the mitigation of the x-ray generation by electron recirculation was studied by varying the volume of a low-Z backing. The simulation results show that the minimum dimension of a CH backing for a 100 μm thick Cu foil with a 1.0 MeV slope electron beam is either a 500 μm thick CH with a large surface area or a 1.0 mm surface area with a longer than 650 μm thickness. Second, the temporal evolution of the x-ray generation for targets with and without electron recirculation was studied. The time history of the integrated x-ray photons over 70 and 200 keV, relevant to broadband x-ray radiography, showed that the x-ray intensity from an isolated Cu foil is 8~10 times longer than that without electron recirculation, which could cause blurring in a radiographic image of a rapidly evolving object (e.g., fusion implosion core).

The benchmarked LSP code was further used to design and optimize a hard x-ray source for x-ray radiography of magnetically compressed Al rod at ZPPL. In this study, the intensity of angularly resolved broadband x-ray radiation was calculated for various thicknesses of an Ag foil. It is found that changing the backlighting direction from the edge-on to the forward direction could increase the x-ray intensity on IP by a factor of 3

with a 10 μm thick foil. These results could be used for a baseline design of an x-ray source target for a future x-ray radiography experiment on Zebra.

The fast electron characterization demonstrated in this thesis was performed only for a peak laser intensity of 2×10^{19} W/cm^2. Future work includes applications of the characterization technique for fast electrons generated by high-intensity and high-energy lasers at recently constructed petawatt-class short-pulse laser facilities worldwide. A fast electron spectrum will have multiple temperature slopes as the peak intensity increases. The 3D LSP hybrid modeling can incorporate an electron energy distribution of multiple slope temperatures. The code can also readily simulate fast electrons generated by a high-power femtosecond laser. Once a laser pulse is longer than a few picoseconds, this modeling approach may be inapplicable because the duration of fast electron generation in the laser-plasma interaction becomes long enough such that fast electrons recirculated back from the target rear can be accelerated by the laser's ponderomotive force multiple times, generating so-called super-ponderomotive electrons. An explicit particle-in-cell code running on state-of-the-art clusters and/or graphic processing units (GPU) could self-consistently simulate multiple-picosecond laser-plasma interaction, fast electron production, and subsequent bremsstrahlung generation.

BIBLIOGRAPHY

1 T. H. Maiman, Nature 187, 493 (1960).

2 F. J. McClung and R. W. Hellwarth, J. Appl. Phys. 33, 828 (1962).

3 L. E. Hargrove, R. L. Fork, and M. A. Pollack, Appl. Phys. Lett. 5, 4 (1964).

4 D. Strickland and G. Mourou, Opt. Commun. 56, 219 (1985).

5 https://www.lle.rochester.edu/index.php/1985/03/01/chirped-pulse-amplification/

6 I.N. Ross, P. Matousek, M. Towrie, A.J. Langley, and J.L. Collier, Opt. Commun. 144, 125 (1997).

7 C.N. Danson, C. Haefner, J. Bromage, T. Butcher, J.C.F. Chanteloup, E.A. Chowdhury, A. Galvanauskas, L.A. Gizzi, J. Hein, D.I. Hillier, N.W. Hopps, Y. Kato, E.A. Khazanov, R. Kodama, G. Korn, R. Li, Y. Li, J. Limpert, J. Ma, C.H. Nam, D. Neely, D. Papadopoulos, R.R. Penman, L. Qian, J.J. Rocca, A.A. Shaykin, C.W. Siders, C. Spindloe, S. Szatmári, R.M.G.M. Trines, J. Zhu, P. Zhu, and J.D. Zuegel, High Power Laser Sci. Eng. 7, (2019).

8 X. Zeng, K. Zhou, Y. Zuo, Q. Zhu, J. Su, X. Wang, X. Wang, X. Huang, X. Jiang, D. Jiang, Y. Guo, N. Xie, S. Zhou, Z. Wu, J. Mu, H. Peng, and F. Jing, Opt. Lett. 42, 2014 (2017).

9 J.W. Yoon, Y.G. Kim, I.W. Choi, J.H. Sung, H.W. Lee, S.K. Lee, and C.H. Nam, Optica 8, 630 (2021).

10 C. Radier, O. Chalus, M. Charbonneau, S. Thambirajah, G. Deschamps, S. David, J. Barbe, E. Etter, G. Matras, S. Ricaud, V. Leroux, C. Richard, F. Lureau, A. Baleanu, R. Banici, A. Gradinariu, C. Caldararu, C. Capiteanu, A. Naziru, B. Diaconescu, V. Iancu, R. Dabu, D. Ursescu, I. Dancus, C.A. Ur, K.A. Tanaka, and N.V. Zamfir, High Power Laser Sci. Eng. 10, 1 (2022).

11 B. Shen, Z. Bu, J. Xu, T. Xu, L. Ji, R. Li, and Z. Xu, Plasma Phys. Control. Fusion 60, (2018).

12 https://zeus.engin.umich.edu

13 P.P. Wiewior, A. Astanovitskiy, G. Aubry, S. Batie, J. Caron, O. Chalyy, T. Cowan, C. Haefner, B. Le Galloudec, N. Le Galloudec, D. MacAulay, V. Nalajala, G. Pettee, S. Samek, Y. Stepanenko, and J. Vesco, J. Fusion Energy 28, 218 (2009).

14 X. Wang, R. Zgadzaj, N. Fazel, Z. Li, S.A. Yi, X. Zhang, W. Henderson, Y.Y. Chang, R. Korzekwa, H.E. Tsai, C.H. Pai, H. Quevedo, G. Dyer, E. Gaul, M. Martinez, A.C. Bernstein, T. Borger, M. Spinks, M. Donovan, V. Khudik, G. Shvets, T. Ditmire, and M.C. Downer, Nat. Commun. 4, (2013).

15 S.C. Wilks, A.B. Langdon, T.E. Cowan, M. Roth, M. Singh, S. Hatchett, M.H. Key, D. Pennington, A. MacKinnon, and R.A. Snavely, Phys. Plasmas 8, 542 (2001).

16 A. Macchi, F. Cattani, T. V. Liseykina, and F. Cornolti, Phys. Rev. Lett. 94, 2 (2005).

17 T. V. Liseikina and A. MacChi, Appl. Phys. Lett. 91, (2007).

18 L. Yin, B.J. Albright, B.M. Hegelich, K.J. Bowers, K.A. Flippo, T.J.T. Kwan, and J.C. Fernández, Phys. Plasmas 14, (2007).

19 J. Denavit, Phys. Rev. Lett. 69, 3052 (1992).

20 T.D. Malouff, A. Mahajan, S. Krishnan, C. Beltran, D.S. Seneviratne, and D.M. Trifiletti, Front. Oncol. 10, 1 (2020).

21 J. Badziak and J. Domański, Plasma Phys. Control. Fusion 63, (2021).

22 N. Maskil and M. Deutsch, Phys. Rev. A 37, 2947 (1988).

23 A. Macchi, M. Borghesi, and M. Passoni, Rev. Mod. Phys. 85, 751 (2013).

24 J. Nuckolls, L. Wood, A. Thiessen, and G. Zimmerman, Nature 239, 139 (1972).

25 U. Zastrau, P. Audebert, V. Bernshtam, E. Brambrink, T. Kämpfer, E. Kroupp, R. Loetzsch, Y. Maron, Y. Ralchenko, H. Reinholz, G. Röpke, A. Sengebusch, E. Stambulchik, I. Uschmann, L. Weingarten, and E. Förster, Phys. Rev. E - Stat. Nonlinear, Soft Matter Phys. 81, 1 (2010).

26 A. Schönlein, G. Boutoux, S. Pikuz, L. Antonelli, D. Batani, A. Debayle, A. Franz, L. Giuffrida, J.J. Honrubia, J. Jacoby, D. Khaghani, P. Neumayer, O.N. Rosmej, T. Sakaki, J.J. Santos, and A. Sauteray, Epl 114, (2016).

27 R.F. Post, Rev. Mod. Phys. 28, 338 (1956).

28 H. Abu-shawareb, Phys. Rev. Lett. 129, 75001 (2022).

29 https://www.llnl.gov/news/national-ignition-facility-achieves-fusion-ignition

30 M. Tabak, J. Hammer, M.E. Glinsky, W.L. Kruer, S.C. Wilks, J. Woodworth, E.M. Campbell, M.D. Perry, and R.J. Mason, Phys. Plasmas 1, 1626 (1994).

31 C.D. Chen, P.K. Patel, D.S. Hey, A.J. MacKinnon, M.H. Key, K.U. Akli, T. Bartal, F.N. Beg, S. Chawla, H. Chen, R.R. Freeman, D.P. Higginson, A. Link, T.Y. Ma, A.G. MacPhee, R.B. Stephens, L.D. Van Woerkom, B. Westover, and M. Porkolab, Phys. Plasmas 16, 1 (2009).

32 E.I. Moses, Nucl. Fusion **49**, (2009).

33 R. Kodama, P.A. Norreys, K. Mima, A.E. Dangor, R.G. Evans, H. Fujita, Y. Kitagawa, K. Krushelnick, T. Miyakoshi, N. Miyanaga, T. Norimatsu, S.J. Rose, T. Shozaki, K. Shigemori, A. Sunahara, M. Tampo, K.A. Tanaka, Y. Toyama, T. Yamanaka, and M. Zepf, Nature 412, 798 (2001).

34 R. Kodama, Y. Sentoku, Z.L. Chen, G.R. Kumar, S.P. Hatchett, Y. Toyama, T.E. Cowan, R.R. Freeman, J. Fuchs, Y. Izawa, M.H. Key, Y. Kitagawa, K. Kondo, T. Matsuoka, H. Nakamura, M. Nakatsutsumi, P.A. Horreys, T. Norimatsu, R.A. Snavely, R.B. Stephens, M. Tampo, K.A. Tanaka, and T. Yabuuchi, Nature 432, 1005 (2004).

35 S. Sakata, S. Lee, H. Morita, T. Johzaki, H. Sawada, Y. Iwasa, K. Matsuo, K.F.F. Law, A. Yao, M. Hata, A. Sunahara, S. Kojima, Y. Abe, H. Kishimoto, A. Syuhada, T. Shiroto, A. Morace, A. Yogo, N. Iwata, M. Nakai, H. Sakagami, T. Ozaki, K. Yamanoi, T. Norimatsu, Y. Nakata, S. Tokita, N. Miyanaga, J. Kawanaka, H. Shiraga, K. Mima, H. Nishimura, M. Bailly-Grandvaux, J.J. Santos, H. Nagatomo, H. Azechi, R. Kodama, Y. Arikawa, Y. Sentoku, and S. Fujioka, Nat. Commun. 9, (2018).

36 K. Matsuo, N. Higashi, N. Iwata, S. Sakata, S. Lee, T. Johzaki, H. Sawada, Y. Iwasa, K.F.F. Law, H. Morita, Y. Ochiai, S. Kojima, Y. Abe, M. Hata, T. Sano, H. Nagatomo, A. Sunahara, A. Morace, A. Yogo, M. Nakai, H. Sakagami, T. Ozaki, K. Yamanoi, T. Norimatsu, Y. Nakata, S. Tokita, J. Kawanaka, H. Shiraga, K. Mima, H. Azechi, R. Kodama, Y. Arikawa, Y. Sentoku, and S. Fujioka, Phys. Rev. Lett. 124, 35001 (2020).

37 J.C. Fernandez, B.J. Albright, F.N. Beg, M.E. Foord, B.M. Hegelich, J.J. Honrubia, M. Roth, R.B. Stephens, and L. Yin, Nucl. Fusion 54, (2014).

38 H. Sawada, S. Lee, T. Shiroto, H. Nagatomo, Y. Arikawa, H. Nishimura, T. Ueda, K. Shigemori, A. Sunahara, N. Ohnishi, F.N. Beg, W. Theobald, F. Pérez, P.K. Patel, and S. Fujioka, Appl. Phys. Lett. 108, (2016).

39 R. Tommasini, H.S. Park, P. Patel, B. Maddox, S. Le Pape, S.P. Hatchett, B.A. Remington, M.H. Key, N. Izumi, M. Tabak, J.A. Koch, O.L. Landen, D. Hey, A. MacKinnon, J. Seely, G. Holland, L. Hudson, and C. Szabo, AIP Conf. Proc. 926, 248 (2007).

40 J.F. Seely and E.G. Harris, Phys. Rev. A 7, 1064 (1973).

41 J.P. Freidberg, R.W. Mitchell, R.L. Morse, and L.I. Rudsinski, Phys. Rev. Lett. 28, 795 (1972).

42 F. Brunel, Phys. Rev. Lett. 59, 52 (1987).

43 W.L. Kruer and K. Estabrook, Phys. Fluids 28, 430 (1985).

44 S.C. Wilks, W.L. Kruer, M. Tabak, and A.B. Langdon, Phys. Rev. Lett. 69, 1383 (1992).

45 A.R. Bell, J.R. Davies, S. Guerin, and H. Ruhl, Plasma Phys. Control. Fusion 39, 653 (1997).

46 M.E. Glinsky, Phys. Plasmas 2, 2796 (1995).

47 J.J. Santos, F. Amiranoff, S.D. Baton, L. Gremillet, M. Koenig, E. Martinolli, M. Rabec Le Gloahec, C. Rousseaux, D. Batani, A. Bernardinello, G. Greison, and T. Hall, Phys. Rev. Lett. 89, 25001 (2002).

48 R.P.J. Town, C. Chen, L.A. Cottrill, M.H. Key, W.L. Kruer, A.B. Langdon, B.F. Lasinski, R.A. Snavely, C.H. Still, M. Tabak, D.R. Welch, and S.C. Wilks, Nucl. Instruments Methods Phys. Res. Sect. A Accel. Spectrometers, Detect. Assoc. Equip. 544, 61 (2005).

49 M. Roth and M. Schollmeier, Cern Yellow Reports 1, 231 (2016).

50 T. Yabuuchi, B.S. Paradkar, M.S. Wei, J.A. King, F.N. Beg, R.B. Stephens, N. Nakanii, M. Hatakeyama, H. Habara, K. Mima, K.A. Tanaka, and J.T. Larsen, Phys. Plasmas 17, (2010).

51 H. Chen, P.K. Patel, D.F. Price, B.K. Young, P.T. Springer, R. Berry, R. Booth, C. Bruns, and D. Nelson, Rev. Sci. Instrum. 74, 1551 (2003).

52 R.B. Stephens, R.A. Snavely, Y. Aglitskiy, F. Amiranoff, C. Andersen, D. Batani, S.D. Baton, T. Cowan, R.R. Freeman, T. Hall, S.P. Hatchett, J.M. Hill, M.H. Key, J.A. King, J.A. Koch, M. Koenig, A.J. MacKinnon, K.L. Lancaster, E. Martinolli, P. Norreys, E. Perelli-Cippo, M. Rabec Le Gloahec, C. Rousseaux, J.J. Santos, and F. Scianitti, Phys. Rev. E - Stat. Physics, Plasmas, Fluids, Relat. Interdiscip. Top. 69, 7 (2004).

53 C.D. Chen, J.A. King, M.H. Key, K.U. Akli, F.N. Beg, H. Chen, R.R. Freeman, A. Link, A.J. MacKinnon, A.G. MacPhee, P.K. Patel, M. Porkolab, R.B. Stephens, and L.D. Van Woerkom, Rev. Sci. Instrum. 79, 529 (2008).

54 L. Gremillet, F. Amiranoff, S.D. Baton, J.-C. Gauthier, M. Koenig, E. Martinolli, F. Pisani, G. Bonnaud, C. Lebourg, C. Rousseaux, C. Toupin, A. Antonicci, D. Batani, A. Bernardinello, T. Hall, D. Scott, P. Norreys, H. Bandulet, and H. Pépin, Phys. Rev. Lett. 83, 5015 (1999).

55 K.L. Lancaster, J.S. Green, D.S. Hey, K.U. Akli, J.R. Davies, R.J. Clarke, R.R. Freeman, H. Habara, M.H. Key, R. Kodama, K. Krushelnick, C.D. Murphy, M. Nakatsutsumi, P. Simpson, R. Stephens, C. Stoeckl, T. Yabuuchi, M. Zepf, and P.A. Norreys, Phys. Rev. Lett. 98, 1 (2007).

56 M. Zepf, E.L. Clark, K. Krushelnick, F.N. Beg, C. Escoda, A.E. Dangor, M.I.K. Santala, M. Tatarakis, I.F. Watts, P.A. Norreys, R.J. Clarke, J.R. Davies, M.A. Sinclair, R.D. Edwards, T.J. Goldsack, I. Spencer, and K.W.D. Ledingham, Phys. Plasmas 8, 2323 (2001).

57 S.P. Hatchett, C.G. Brown, T.E. Cowan, E.A. Henry, J.S. Johnson, M.H. Key, J.A. Koch, A.B. Langdon, B.F. Lasinski, R.W. Lee, A.J. Mackinnon, D.M. Pennington, M.D. Perry, T.W. Phillips, M. Roth, T.C. Sangster, M.S. Singh, R.A. Snavely, M.A. Stoyer, S.C. Wilks, and K. Yasuike, Phys. Plasmas 7, 2076 (2000).

58 F.N. Beg, A.R. Bell, A.E. Dangor, C.N. Danson, A.P. Fews, M.E. Glinsky, B.A. Hammel, P. Lee, P.A. Norreys, and M. Tatarakis, Phys. Plasmas 4, 447 (1997).

59 J.J. Honrubia and J. Meyer-Ter-Vehn, Plasma Phys. Control. Fusion 51, (2009).

60 J.S. Green, V.M. Ovchinnikov, R.G. Evans, K.U. Akli, H. Azechi, F.N. Beg, C. Bellei, R.R. Freeman, H. Habara, R. Heathcote, M.H. Key, J.A. King, K.L. Lancaster, N.C. Lopes, T. Ma, A.J. MacKinnon, K. Markey, A. McPhee, Z. Najmudin, P. Nilson, R. Onofrei, R. Stephens, K. Takeda, K.A. Tanaka, W. Theobald, T. Tanimoto, J. Waugh, L. Van Woerkom, N.C. Woolsey, M. Zepf, J.R. Davies, and P.A. Norreys, Phys. Rev. Lett. 100, 1 (2008).

61 M. Storm, A.A. Solodov, J.F. Myatt, D.D. Meyerhofer, C. Stoeckl, C. Mileham, R. Betti, P.M. Nilson, T.C. Sangster, W. Theobald, and C. Guo, Phys. Rev. Lett. 102, 235004 (2009).

62 S.D. Baton, J.J. Santos, F. Amiranoff, H. Popescu, L. Gremillet, M. Koenig, E. Martinolli, O. Guilbaud, C. Rousseaux, M. Rabec Le Gloahec, T. Hall, D. Batani, E. Perelli, F. Scianitti, and T.E. Cowan, Phys. Rev. Lett. 91, 105001 (2003).

63 C.D. Armstrong, C.M. Brenner, E. Zemaityte, G.G. Scott, D.R. Rusby, G. Liao, H. Liu, Y. Li, Z. Zhang, Y. Zhang, B. Zhu, P. Bradford, N.C. Woolsey, P. Oliveira, C. Spindloe, W. Wang, P. McKenna, and D. Neely, Plasma Phys. Control. Fusion 61, (2019).

64 D.J. Strozzi, M. Tabak, D.J. Larson, L. Divol, A.J. Kemp, C. Bellei, M.M. Marinak, and M.H. Key, Phys. Plasmas 19, (2012).

65 A.R. Bell, J.R. Davies, and S.M. Guerin, Phys. Rev. E - Stat. Physics, Plasmas, Fluids, Relat. Interdiscip. Top. 58, 2471 (1998).

66 R.H.H. Scott, F. Pérez, M.J.V. Streeter, E.L. Clark, J.R. Davies, H.P. Schlenvoigt, J.J. Santos, S. Hulin, K.L. Lancaster, F. Dorchies, C. Fourment, B. Vauzour, A.A. Soloviev, S.D. Baton, S.J. Rose, and P.A. Norreys, New J. Phys. 15, (2013).

67 P.M. Nilson, A.A. Solodov, J.F. Myatt, W. Theobald, P.A. Jaanimagi, L. Gao, C. Stoeckl, R.S. Craxton, J.A. Delettrez, B. Yaakobi, J.D. Zuegel, B.E. Kruschwitz, C. Dorrer, J.H. Kelly, K.U. Akli, P.K. Patel, A.J. MacKinnon, R. Betti, T.C. Sangster, and D.D. Meyerhofer, Phys. Plasmas 18, (2011).

68 B. Westover, C.D. Chen, P.K. Patel, H. McLean, and F.N. Beg, Phys. Plasmas **21**, 031212 (2014).

69 Developed by Fujifilm Corporation.

70 H. Chen, N.L. Back, T. Bartal, F.N. Beg, D.C. Eder, A.J. Link, A.G. MacPhee, Y. Ping, P.M. Song, A. Throop, and L. Van Woerkom, Rev. Sci. Instrum. **79**, (2008).

71 B. Westover, C.D. Chen, P.K. Patel, M.H. Key, H. McLean, R. Stephens, and F.N. Beg, Phys. Plasmas 18, 1 (2011).

72 C.D. Chen, A.J. Kemp, F. Pérez, A. Link, F.N. Beg, S. Chawla, M.H. Key, H. McLean, A. Morace, Y. Ping, A. Sorokovikova, R.B. Stephens, M. Streeter, B. Westover, and P.K. Patel, Phys. Plasmas 20, (2013).

73 H. Sawada, T.S. Daykin, T.M. Hutchinson, B.S. Bauer, V. V. Ivanov, F.N. Beg, H. Chen, G.J. Williams, and H.S. McLean, Phys. Plasmas 26, 083104 (2019).

74 H. Sawada, C.M. Salinas, F.N. Beg, H. Chen, A.J. Link, H.S. McLean, P.K. Patel, Y. Ping, and G.J. Williams, Plasma Phys. Control. Fusion 62, (2020).

75 T.S. Daykin, H. Sawada, Y. Sentoku, F.N. Beg, H. Chen, H.S. McLean, A.J. Link, P.K. Patel, and Y. Ping, Phys. Plasmas 25, (2018).

76 J.M. Dawson, Rev. Mod. Phys. 55, 403 (1983).

77 T.P. Hughes, R.E. Clark, and S.S. Yu, Phys. Rev. Spec. Top. - Accel. Beams 2, 1 (1999).

78 D.R. Welch, D. V. Rose, M.E. Cuneo, R.B. Campbell, and T.A. Mehlhorn, Phys. Plasmas 13, (2006).

79 M.S. Wei, A.A. Solodov, J. Pasley, R.B. Stephens, D.R. Welch, and F.N. Beg, Phys. Plasmas 15, (2008).

80 D.R. Welch, D. V. Rose, B. V. Oliver, and R.E. Clark, Nucl. Instruments Methods Phys. Res. Sect. A Accel. Spectrometers, Detect. Assoc. Equip. 464, 134 (2001).

81 H. Hirayama, Y. Namito, A. F. Bielajew, S. J. Wilderman, and W. R. Nelson, "The EGS5 code system," SLAC-R-730 and KEK Report 2005- 8 (SLAC National Accelerator Laboratory and High Energy Accelerator Research Organization, Menlo Park, USA and Tsukuba, Japan, 2005).

82 T. Sato, Y. Iwamoto, S. Hashimoto, T. Ogawa, T. Furuta, S.-I. Abe, T. Kai, P.-E. Tsai, N. Matsuda, H. Iwase, N. Shigyo, L. Sihver, and K. Niita, (2018).

83 https://www.nist.gov/pml/x-ray-mass-attenuation-coefficients

84 H. Sawada, Y. Sentoku, T. Yabuuchi, U. Zastrau, E. Förster, F.N. Beg, H. Chen, A.J. Kemp, H.S. McLean, P.K. Patel, and Y. Ping, Phys. Rev. Lett. 122, 2 (2019).

85 A. Link, R.R. Freeman, D.W. Schumacher, and L.D. Van Woerkom, Phys. Plasmas 18, 053107 (2011).

86 D.R. Rusby, C.D. Armstrong, G.G. Scott, M. King, P. McKenna, and D. Neely, High Power Laser Sci. Eng. (2019).

87 P. Mora, Phys. Rev. Lett. 90, 185002 (2003)

88 M. Li, H. An, G. Hu, J. Xiong, A. Lei, Z. Xie, C. Wang, W. Wang, Z. Zhang, and L. Huang, Phys. Plasmas 29, 013107 (2022).

89 S. Atzeni, A Schiavi, and J.R. Davies, Plasma Phys. Control. Fusion 51, 015016 (2009)

90 D. Groom and S. Klein, The European Physical Journal C-Particles and Fields 15, 163–173 (2000)

91 S.M. Seltzer and M.J. Berger, IEEE Trans. Nucl. Sci. 39, 1025 (1992).

92 B. Borm, D. Khaghani, and P. Neumayer, Phys. Plasmas 26, 023109 (2019).

93 K.D. Xiao, C.T. Zhou, K. Jiang, Y.C. Yang, R. Li, H. Zhang, B. Qiao, T.W. Huang, J.M. Cao, T.X. Cai, M.Y. Yu, S.C. Ruan, and X.T. He, Phys. Plasmas 25, 023103 (2018).

94 R. Tommasini, A. MacPhee, D. Hey, T. Ma, C. Chen, N. Izumi, W. Unites, A. MacKinnon, S.P. Hatchett, B. a Remington, H.S. Park, P. Springer, J. a Koch, O.L. Landen, J. Seely, G. Holland, and L. Hudson, Rev. Sci. Instrum. 79, 10E901 (2008).

95 R. Tommasini, C. Bailey, D.K. Bradley, M. Bowers, H. Chen, J.M. Di Nicola, P. Di Nicola, G. Gururangan, G.N. Hall, C.M. Hardy, D. Hargrove, M. Hermann, M. Hohenberger, J.P. Holder, W. Hsing, N. Izumi, D. Kalantar, S. Khan, J. Kroll, O.L. Landen, J. Lawson, D. Martinez, N. Masters, J.R. Nafziger, S.R. Nagel, A. Nikroo, J. Okui, D. Palmer, R. Sigurdsson, S. Vonhof, R.J. Wallace, and T. Zobrist, Phys. Plasmas 24, 053104 (2017).

96 T.J. Awe, B.S. Bauer, S. Fuelling, and R.E. Siemon, Phys. Rev. Lett. 104, 1 (2010).

97 S. Buitron. (2023). Monte Carlo simulations of radiation shielding design for broadband x-ray radiography at Zebra Pulsed Power Laboratory. [Unpublished senior thesis]. University of Nevada, Reno.

98 H.S. Park, D.M. Chambers, H.K. Chung, R.J. Clarke, R. Eagleton, E. Giraldez, T. Goldsack, R. Heathcote, N. Izumi, M.H. Key, J.A. King, J.A. Koch, O.L. Landen, A. Nikroo, P.K. Patel, D.F. Price, B.A. Remington, H.F. Robey, R.A. Snavely, D.A. Steinman, R.B. Stephens, C. Stoeckl, M. Storm, M. Tabak, W. Theobald, R.P.J. Town, J.E. Wickersham, and B.B. Zhang, Phys. Plasmas **13**, (2006).